Range of validity of an extended WKB theory for atmospheric gravity waves: one-dimensional and two-dimensional case

Felix Rieper[1],[†], U. Achatz[1] and R. Klein[2]

[1]Institut für Atmosphäre und Umwelt, Goethe Universität, D-60438 Frankfurt am Main, Germany
[2]Institut für Mathematik, Freie Universität, 14195 Berlin, Germany

A computational model of the pseudo-incompressible equations is used to probe the range of validity of an extended Wentzel–Kramers–Brillouin theory (XWKB), previously derived through a distinguished limit of a multiple-scale asymptotic analysis of the Euler or pseudo-incompressible equations of motion, for gravity-wave packets at large amplitudes. The governing parameter of this analysis had been the scale-separation ratio ε between the gravity wave and both the large-scale potential-temperature stratification and the large-scale wave-induced mean flow. A novel feature of the theory had been the non-resonant forcing of higher harmonics of an initial wave packet, predominantly by the large-scale gradients in the gravity-wave fluxes. In the test cases considered a gravity-wave packet is propagating upwards in a uniformly stratified atmosphere. Large-scale winds are induced by the wave packet, and possibly exert a feedback on the latter. In the limit $\varepsilon \ll 1$ all predictions of the theory can be validated. The larger ε is the more the transfer of wave energy to the mean flow is underestimated by the theory. The numerical results quantify this behaviour but also show that, qualitatively, XWKB remains valid even when the gravity-wave wavelength approaches the spatial scale of the wave-packet amplitude. This includes the prevalence of first and second harmonics and the smallness of harmonics with wave number higher than two. Furthermore, XWKB predicts for the vertical momentum balance an additional leading-order buoyancy term in Euler and pseudo-incompressible theory, compared with the anelastic theory. Numerical tests show that this term is relatively large with up to 30 % of the total balance. The practical relevance of this deviation remains to be assessed in future work.

Key words: atmospheric flows, internal waves, stratified flows

1. Introduction

Gravity waves contribute significantly to the mesoscale dynamics of the atmosphere (e.g. Fritts & Alexander 2003; Kim, Eckermann & Chun 2003; Alexander *et al.* 2010). Being generated by various processes, mostly in the troposphere, they can propagate over large distances until they break and by this or other nonlinear interactions

† Present address: Deutscher Wetterdienst, 63067 Offenbach, Germany. Email address for correspondence: felix.rieper@dwd.de

can have an influence on the momentum and energy budget of the large-scale flow. Corresponding effects must be taken into account in both weather prediction and in climate simulations. This gravity-wave influence must be parameterized because the time and length scale of most parts of the gravity-wave spectrum are too small to be resolved explicitly. Prominent examples of parameterization were proposed, for example, by Lindzen (1981), Holton (1982), Medvedev & Klaassen (1995), Hines (1997) and Alexander & Dunkerton (1999). Most of these approaches make use of the results obtained from Wentzel–Kramers–Brillouin (WKB) theory (Bretherton 1966; Grimshaw 1975a; Müller 1976) for gravity-wave packets (GWPs). This approach assumes a small variation of the wave properties frequency, wave number and amplitude over a wavelength and a period. It leads to a closed system of equations describing the propagation of frequency and wave number along rays, the conservative transport of wave action and the interaction with the large-scale flow.

An extension of the classical WKB theory for gravity waves was presented by Achatz, Klein & Senf (2010) and Klein (2011), named extended WKB (XWKB). It was derived through a distinguished limit within a multiscale asymptotic analysis (e.g. Klein 2010) of the governing equations. The small-scale separation parameter ε was assumed to characterize the scale ratio between the gravity wave and both its large-scale envelope and the large-scale atmosphere entropy stratification. The amplitude of the basic wave itself is assumed to be large, i.e. $O(1)$ with regards to the static-instability threshold, and higher harmonics, predominantly forced by large-scale gradients in the gravity-wave fluxes, are found at $O(\varepsilon)$ amplitude. The nonlinear forcing of the second harmonic is predicted, while even higher harmonics are found to be negligible at the considered order in ε. As gravity-wave parameterizations often push WKB theory to its limits by applying it to cases where the scale separation is not so significant any more, the question arises how well WKB theory, and its nonlinear extension, perform as the scale-separation parameter approaches values of order $O(1)$. Moreover, the WKB theory derivable as a distinguished limit of the governing equations differs as either the pseudo-incompressible theory (Durran 1989) is taken as the starting point, on the one hand, or the anelastic equations (Lipps & Hemler 1982), on the other hand. The former lead to the same XWKB theory as the complete compressible Euler equations while the latter yield different predictions of the second harmonic and also miss a, so far not quantified, wave-related correction of vertical-momentum balance. Since the pseudo-incompressible system has a divergence constraint that is much harder to solve it was worth questioning why we do not go on working with the classical, much simpler anelastic system as long as there is often no noticeable difference in the solution (e.g. Klein 2009; Smolarkiewicz & Szmelter 2011). In the work reported here we have set out to examine the following two main questions. (i) How well does the XWKB theory perform in comparison with the more general numerical solutions of the pseudo-incompressible equations? (ii) How much does this performance depend on the scale-separation parameter being small and on the conditions for a distinguished limit being met? Beyond this we also want to give a first assessment of how large the deviations of the pseudo-incompressible WKB theory can be from its anelastic counterpart.

This paper is organized as follows. In §2 we present the governing equations of XWKB (Achatz *et al.* 2010). For the convenience of potential users they are here given in dimensional form for the first time. Their implementation with a ray tracer model is explained in §3. The validation of the WKB theory is then split into two parts: in §4 we compare the full model with the ray tracer for a one-dimensional GWP, i.e. with a Gaussian profile only depending on the vertical coordinate; in §5

we present the results for the more general case of a horizontally periodic chain of two-dimensional GWP with a Gaussian profile depending on horizontal and vertical coordinate. We finish the paper with a discussion of the results in § 6.

2. Governing WKB equations

In this section we summarize the governing equations of XWKB in dimensional form. For more details on the multiscale asymptotic analysis of the two-dimensional Euler equations without rotation we refer the reader to Achatz *et al.* (2010) who use as a starting point either the Euler equations

$$\frac{Du}{Dt} + c_p\theta\frac{\partial\pi}{\partial x} = 0 \tag{2.1}$$

$$\frac{Dw}{Dt} + c_p\theta\frac{\partial\pi}{\partial z} = -g \tag{2.2}$$

$$\frac{D\theta}{Dt} = 0 \tag{2.3}$$

$$\frac{D\pi}{Dt} + \frac{R}{c_v}\pi\nabla\cdot\boldsymbol{v} = 0 \tag{2.4}$$

or the pseudo-incompressible equations

$$\frac{Du}{Dt} + c_p\theta\frac{\partial\pi}{\partial x} = 0 \tag{2.5}$$

$$\frac{Dw}{Dt} + c_p\theta\frac{\partial\pi}{\partial z} = -g \tag{2.6}$$

$$\frac{D\theta}{Dt} = 0 \tag{2.7}$$

$$\nabla\cdot(\overline{\rho}\overline{\theta}\boldsymbol{v}) = 0. \tag{2.8}$$

With the wind vector $\boldsymbol{v} = (u, w)$ and its horizontal and vertical components u and w, respectively. The material derivative is

$$\frac{D}{Dt} = \frac{\partial}{\partial t} + u\frac{\partial}{\partial x} + w\frac{\partial}{\partial z}. \tag{2.9}$$

The specific heat coefficients at constant pressure and volume are c_p and c_v, respectively, and $R = c_p - c_v$ is the gas constant. The Exner pressure is given by $\pi = (p/p_0)^{R/c_p}$ for some reference value p_0. The potential temperature satisfies $\theta = T/\pi$, where T is the temperature. Here $\overline{\rho}$ and $\overline{\theta}$ denote density and potential temperature of a hydrostatic reference atmosphere.

2.1. *The XWKB ansatz*

For spatial extent and temporal change of the wave packet we introduce the compressed spatial coordinates ζ and χ along with the slow time coordinate τ

$$\zeta = \varepsilon z \tag{2.10}$$

$$\chi = \varepsilon x \tag{2.11}$$

$$\tau = \varepsilon t \tag{2.12}$$

with the small parameter $\varepsilon = L/H_\theta = 1/(KH_\theta)$ relating the wavelength L, or rather the inverse of the wave number K, to the isothermal potential-temperature height H_θ. Here x and z are coordinates scaled with $L = 1/K$ and, therefore, ζ and χ are scaled with the isothermal potential temperature scale height. Note that the present theory assumes isotropic spatial scaling so that it focuses on non-hydrostatic rather than hydrostatic waves. For the general results of the multiscale asymptotic ansatz introduced to the Euler equations, the pseudo-incompressible equations (Durran 1989) and the anelastic equations (Lipps & Hemler 1982) we refer to Achatz *et al.* (2010). Here we solely focus on the XWKB ansatz considering the large-amplitude regime. Using the polarization relations for linear gravity waves it can be shown that the ratio between the potential-temperature fluctuations in a wave, with an amplitude just marginally below the static instability limit, and the large-scale background-atmosphere potential temperature is $O(\varepsilon)$, while the corresponding ratio for the Exner pressure is $O(\varepsilon^2)$. Thus, for the non-dimensional fields, denoted by $(\hat{\ })$, the ansatz

$$\hat{u} = \tilde{u}^{(0)} \tag{2.13}$$

$$\hat{w} = \tilde{w}^{(0)} \tag{2.14}$$

$$\hat{\theta} = \hat{\theta}^{(0)} + \varepsilon \tilde{\theta}^{(1)} \tag{2.15}$$

$$\hat{\pi} = \hat{\pi}^{(0)} + \varepsilon^2 \tilde{\pi}^{(2)} \tag{2.16}$$

is used, where $\hat{\theta}^{(0)}$ and $\hat{\pi}^{(0)}$ are potential temperature and Exner pressure of the large-scale hydrostatic background atmosphere, and all dynamic fields, composed of the wave and all fields influenced by it, either large-scale flow or higher harmonics, are denoted by $(\tilde{\ })$. They are decomposed as

$$
\begin{pmatrix} \tilde{u}^{(0)} \\ \tilde{w}^{(0)} \\ \tilde{\theta}^{(1)} \\ \tilde{\pi}^{(2)} \end{pmatrix} = \begin{pmatrix} \hat{U}_0^{(0)} \\ \hat{W}_0^{(0)} \\ \hat{\Theta}_0^{(1)} \\ \hat{\Pi}_0^{(2)} \end{pmatrix} (\tau, \chi, \zeta) + \operatorname{Re}\left[\begin{pmatrix} \hat{U}_1^{(0)} \\ \hat{W}_1^{(0)} \\ \hat{\Theta}_1^{(1)} \\ \hat{\Pi}_1^{(2)} \end{pmatrix} (\tau, \chi, \zeta) \exp\left(i\frac{\phi(\tau, \chi, \zeta)}{\varepsilon} \right) \right]
$$

$$
+ \varepsilon \left[\begin{pmatrix} \hat{U}_0^{(1)} \\ \hat{W}_0^{(1)} \\ \hat{\Theta}_0^{(2)} \\ \hat{\Pi}_0^{(3)} \end{pmatrix} (\tau, \chi, \zeta) + \operatorname{Re}\sum_{\alpha=1}^{\infty} \begin{pmatrix} \hat{U}_\alpha^{(1)} \\ \hat{W}_\alpha^{(1)} \\ \hat{\Theta}_\alpha^{(2)} \\ \hat{\Pi}_\alpha^{(3)} \end{pmatrix} (\tau, \chi, \zeta) \exp\left(i\alpha \frac{\phi(\tau, \chi, \zeta)}{\varepsilon} \right) \right]
$$

$$+ o(\varepsilon). \tag{2.17}$$

The notation has been chosen so that the upper index always indicates the effective order in ε, while the lower index denotes the order in the wave-phase factor. Thus, the first part on the right-hand side (RHS) is the leading-order large-scale flow, possibly influenced by the waves (see below), the second the small-scale gravity-wave field with large-scale amplitude and with velocity amplitudes comparable with the strength of the leading-order large-scale wind, the third a next-order modification of the large-scale flow and the last both a next-order modification of the gravity-wave field and higher harmonics induced by the latter. As these turn out to be forced predominantly by large-scale gradients in the gravity-wave fluxes they are $O(\varepsilon)$. A restriction of the theory is that it does not take nonlinear wave–wave interactions (e.g. McComas & Bretherton 1977; Caillol & Zeitlin 2000; Lvov, Polzin & Yokoyama 2012) into account which have been shown by Dunkerton (1987) to be relevant as soon as a gravity wave

propagates into a region where other gravity waves are present. In that regard it can be considered weakly nonlinear, but all other aspects are treated in a large-amplitude framework. Spatial and temporal changes of the rapidly varying phase ϕ/ε give rise to the definition of local frequency and wave vector

$$\omega := -\frac{\partial}{\partial t}\left(\frac{\phi}{\varepsilon}\right) = -\frac{\partial \phi}{\partial \tau} \tag{2.18}$$

$$k := \frac{\partial}{\partial x}\left(\frac{\phi}{\varepsilon}\right) = \frac{\partial \phi}{\partial \chi} \tag{2.19}$$

$$m := \frac{\partial}{\partial z}\left(\frac{\phi}{\varepsilon}\right) = \frac{\partial \phi}{\partial \zeta}. \tag{2.20}$$

It is assumed that at each location there is only one local wave number and frequency. This condition is violated as soon as gravity-wave rays cross, e.g. by wave refraction (Dunkerton 1984). Corresponding extensions of the theory, although important, are left to future work. Inserting the ansatz just described into either the Euler equations or the pseudo-incompressible equations returns the classical linear results at leading order, along with new results for mean flow and higher harmonics at first and higher orders. In the following we present the results of the XWKB approach in dimensional form so that an implementation in a code using SI units is straightforward. Recall that dimensional quantities are designated without a hat $(\hat{\ })$, apart from the intrinsic frequency given by $\hat{\omega} = \omega - kU_0^{(0)} - mW_0^{(0)}$. Note that different results are obtained when the anelastic equations are taken as the starting point (Achatz *et al.* 2010; Klein 2011).

2.2. *Leading-order results*

An important leading-order result from the Exner-pressure equation is that the gravity-wave velocity field is orthogonal to the local wave number, i.e. $kU_1^{(0)} + mW_1^{(0)} = 0$, as in linear Boussinesq theory. This has the consequence, for arbitrary large-scale stratification and large-scale winds, that also the leading-order results from the remaining equations reproduce the classic linear theory. We obtain

$$\underbrace{\begin{pmatrix} -i\hat{\omega} & 0 & 0 & ik \\ 0 & -i\hat{\omega} & -N & im \\ 0 & N & -i\hat{\omega} & 0 \\ ik & im & 0 & 0 \end{pmatrix}}_{M(\hat{\omega},k,m)} \begin{pmatrix} U_1^{(0)} \\ W_1^{(0)} \\ \dfrac{g}{N}\dfrac{\Theta_1^{(1)}}{\theta^{(0)}} \\ \theta^{(0)}c_p\Pi_1^{(2)} \end{pmatrix} = 0 \tag{2.21}$$

where $N = \sqrt{(g/\theta^{(0)})(\mathrm{d}\theta^{(0)}/\mathrm{d}z)}$ is the Brunt–Väisälä frequency corresponding to the stratification of the reference atmosphere. Equation (2.21) has non-trivial solutions if $\det(M) = 0$ so that the intrinsic frequency $\hat{\omega}$ and wave vector $\boldsymbol{k} = (k, m)$ satisfy the gravity-wave dispersion relation

$$\hat{\omega}^2(k, m) = N^2 \frac{k^2}{k^2 + m^2} \tag{2.22}$$

known from Boussinesq theory. As a length scale separation has been assumed between the gravity wave and reference atmosphere, anelastic or pseudo-incompressible deviations in the dispersion relation from the Boussinesq result turn out

to be of higher order in the asymptotics. Note that the impact of the mean horizontal wind, be it modified or induced by the GWP, on the gravity-wave phase is included, as the very definition of frequency and wave number implies the Hamilton–Jacobi equation

$$\frac{\partial \phi}{\partial \tau} + U_0^{(0)} \frac{\partial \phi}{\partial \chi} + \hat{\omega}\left(\frac{\partial \phi}{\partial \chi}, \frac{\partial \phi}{\partial \zeta}\right) = 0 \tag{2.23}$$

where $\hat{\omega}(k, m) = \pm N\sqrt{k^2/(k^2 + m^2)}$. Wave properties are transported along rays defined by the ray equations

$$\left(\frac{\partial}{\partial t} + \boldsymbol{c}_g \cdot \nabla_{(x,z)}\right) k = 0 \tag{2.24a}$$

$$\left(\frac{\partial}{\partial t} + \boldsymbol{c}_g \cdot \nabla_{(x,z)}\right) m = -k\frac{\partial U_0^{(0)}}{\partial z} \tag{2.24b}$$

$$\left(\frac{\partial}{\partial t} + \boldsymbol{c}_g \cdot \nabla_{(x,z)}\right) \omega = k\frac{\partial U_0^{(0)}}{\partial t} \tag{2.24c}$$

where the group velocity is given by

$$\boldsymbol{c}_g = \left(U_0^{(0)} + \frac{\partial \hat{\omega}}{\partial k}, \frac{\partial \hat{\omega}}{\partial m}\right). \tag{2.25}$$

This motivates the calculation of these wave properties using a Lagrangian approach.

The wave action $A = E'/\hat{\omega}$, with E' being wave energy (see below), satisfies a conservation law

$$\frac{\partial A}{\partial t} + \nabla_{(x,z)} \cdot (\boldsymbol{c}_g A) = 0 \tag{2.26}$$

which motivates the calculation of the energy transport using finite-volume methods. Wave 1 amplitudes (i.e. a wave with $\alpha = 1$) can then be derived from the energy relation

$$E' = \frac{1}{2}\rho^{(0)}\left(\frac{B_1^{(1)}}{N}\right)^2 \quad \text{with the buoyancy amplitude } B_1^{(1)} = g\frac{\Theta_1^{(1)}}{\theta^{(0)}} \tag{2.27}$$

along with the polarization relations originating from the solution to (2.21)

$$(U_1^{(0)}, W_1^{(0)}, c_p\theta^{(0)}\Pi_1^{(2)}, \Theta_1^{(1)}) = \left(-\mathrm{i}\frac{m}{k}\frac{\hat{\omega}}{N^2}, \mathrm{i}\frac{\hat{\omega}}{N^2}, -\mathrm{i}\frac{m}{k^2}\frac{\hat{\omega}^2}{N^2}, \frac{\theta^{(0)}}{g}\right) B_1^{(1)}. \tag{2.28}$$

The spatially varying reference density $\rho^{(0)} = \overline{\rho}$ enters in the energy so that wave-action conservation implies the correct, non-Boussinesq, gravity-wave amplitude growth during an upward propagation of a wave packet. A central advantage of WKB theory is that it need no longer resolve separate wave crests and troughs, but only the large-scale dependence of gravity-wave amplitude, wave number and frequency. This potentially leads to a much more efficient description of the gravity-wave impact on the large-scale flow.

2.3. *First-order effects*

2.3.1. *Second harmonics ($\alpha = 2$)*

As the most important result of the nonlinear extensions, once wave 1 is known, the equations for wave 2 (i.e. $\alpha = 2$) with system matrix $M_2 := M(2\hat{\omega}, 2k, 2m)$

$$
M(2\hat{\omega}, 2k, 2m)
\begin{pmatrix}
U_2^{(1)} \\
W_2^{(1)} \\
\dfrac{g}{N}\dfrac{\Theta_2^{(2)}}{\theta^{(0)}} \\
c_p\theta^{(0)}\Pi_2^{(3)}
\end{pmatrix}
=
\begin{pmatrix}
-D_1 U_1^{(0)} - \dfrac{1}{2}\mathrm{i}k\Theta_1^{(1)}c_p\Pi_1^{(2)} \\
-D_1 W_1^{(0)} - \dfrac{1}{2}\mathrm{i}m\Theta_1^{(1)}c_p\Pi_1^{(2)} \\
-\dfrac{g}{N\theta^{(0)}}D_1\Theta_1^{(1)} \\
0
\end{pmatrix}
\tag{2.29}
$$

can be solved, where

$$
D_1 = \frac{1}{2}\left(U_1^{(0)}\frac{\partial}{\partial x} + W_1^{(0)}\frac{\partial}{\partial z} + \mathrm{i}kU_1^{(1)} + \mathrm{i}mW_1^{(1)} \right)
\tag{2.30}
$$

and the next-order wave divergence is given by

$$
\mathrm{i}kU_1^{(1)} + \mathrm{i}mW_1^{(1)} = -\frac{\partial U_1^{(0)}}{\partial x} - \frac{\partial W_1^{(0)}}{\partial z} - \frac{1-\kappa}{\kappa}\frac{W_1^{(0)}}{\pi^{(0)}}\frac{\partial \pi^{(0)}}{\partial z}.
\tag{2.31}
$$

This system of linear equations is invertible since M_2 is non-singular if (2.22) is satisfied. These equations, obtainable both from the Euler equations and from the pseudo-incompressible equations, differ from their anelastic analogue (Klein 2011).

2.3.2. *Higher harmonics ($\alpha > 2$)*

In the multiscale asymptotic analysis, all harmonics with wave number higher than two vanish up to and including first order in ε.

2.3.3. *Mean flow*

Finally the mean flow terms satisfy

$$
\Theta_0^{(1)} = 0
\tag{2.32}
$$

$$
W_0^{(0)} = 0
\tag{2.33}
$$

$$
\frac{\partial U_0^{(0)}}{\partial x} = 0
\tag{2.34}
$$

$$
\frac{\partial U_0^{(0)}}{\partial t} + \theta^{(0)}c_p\frac{\partial \Pi_0^{(2)}}{\partial x}
= -\frac{1}{2\rho^{(0)}}\left\{ \frac{\partial}{\partial x}\left[\rho^{(0)}|U_1^{(0)}|^2 \right] + \frac{\partial}{\partial z}\left[\rho^{(0)}\mathrm{Re}\left(U_1^{(0)}W_1^{(0)*} \right) \right] \right\}
\tag{2.35}
$$

$$
\theta^{(0)}c_p\frac{\partial \Pi_0^{(2)}}{\partial z} - g\frac{\Theta_0^{(2)}}{\theta^{(0)}} + g\frac{|\Theta_1^{(1)}|^2}{2\theta^{(0)2}}
= -\frac{1}{2\rho^{(0)}}\left\{ \frac{\partial}{\partial x}\left[\rho^{(0)}\mathrm{Re}\left(U_1^{(0)}W_1^{(0)*} \right) \right] + \frac{\partial}{\partial z}\left[\rho^{(0)}|W_1^{(0)}|^2 \right] \right\}.
\tag{2.36}
$$

From these equations $U_0^{(0)}$, $\Pi_0^{(2)}$ and $\Theta_0^{(2)}$ can be derived as will be shown in the following section. Most of this is well-known (Bretherton 1966; Grimshaw 1975*a*; Müller 1976), but note that in the last equation (actually the vertical-momentum equation), the last term on the left-hand side is a wave-related modification of the momentum balance which appears both in a WKB theory as derivable from the

Euler equations and in its pseudo-incompressible counterpart, but not however in the anelastic WKB.

For later reference we also note that the equations reproduce in the horizontally homogeneous case the wave-induced mean flow (Grimshaw 1975*b*) which plays an important role in the modulational instability of GWPs with infinite horizontal extent (Sutherland 2006; Dosser & Sutherland 2011). From the polarization relations (2.28), the dispersion relation (2.22) and the group-velocity definition one readily finds that the vertical momentum flux can be rewritten

$$\frac{\rho^{(0)}}{2}\mathrm{Re}\left(U_1^{(0)}W_1^{(0)*}\right) = c_{gz}kA \tag{2.37}$$

with c_{gz} the vertical group-velocity component. In the horizontally homogeneous case, frequency, wave number and all amplitudes are independent of x. Under these conditions the prognostic equation (2.24) for horizontal wave number and the wave-action equation (2.26) lead to a conservation equation

$$\frac{\partial}{\partial t}(kA) + \frac{\partial}{\partial z}(c_{gz}kA) = 0 \tag{2.38}$$

for horizontal pseudo-momentum kA, while the horizontal momentum equation (2.35) becomes, with (2.37),

$$\frac{\partial}{\partial t}\left(\rho^{(0)}U_0^{(0)}\right) + \frac{\partial}{\partial z}(c_{gz}kA) = 0. \tag{2.39}$$

From this follows

$$\rho^{(0)}U_0^{(0)}(z,t) = (kA)(z,t) + \rho^{(0)}U_0^{(0)}(z,0) - (kA)(z,0). \tag{2.40}$$

Thus, in regions with zero initial pseudo-momentum, deviations of the mean horizontal flow from its initial value are given by the pseudo-momentum transported there by the gravity waves. Again using the polarization relations (2.28), the latter can also be expressed via vorticity $\zeta = imU_1^{(0)} - ikW_1^{(0)}$ and vertical displacement $\xi = iW_1^{(0)}/\hat{\omega}$ as

$$kA = -\tfrac{1}{2}\mathrm{Re}\left(\zeta\xi^*\right). \tag{2.41}$$

Obviously the frequency $\omega = \hat{\omega} + kU_0^{(0)}$ is Doppler-shifted by the mean flow, be it present initially or induced by the waves.

3. Implementation

From a fluid-dynamical view point we have adopted an Euler–Lagrangian mixed transport method for the solution to (2.24) and (2.26). The wave action A is treated as a conservative variable in a finite-volume method using second-order monotone upstream-centred schemes for conservation laws (MUSCL) with a modern total variation diminishing (TVD) limiter (Toro 1999; Kemm 2010). The rays are transported in a Lagrangian manner. Once the wave action is known in a finite-volume cell, the wave 1 amplitude can be calculated using (2.27) and (2.28). We use a third-order Runge–Kutta scheme (e.g. Durran 1999) for the time stepping in both the integration of the ray equations and in that for the wave action. The wave 2 amplitudes follow from inverting (2.29) and the mean flow can be deduced from (2.32) to (2.36). Boundary conditions are always periodic in the horizontal.
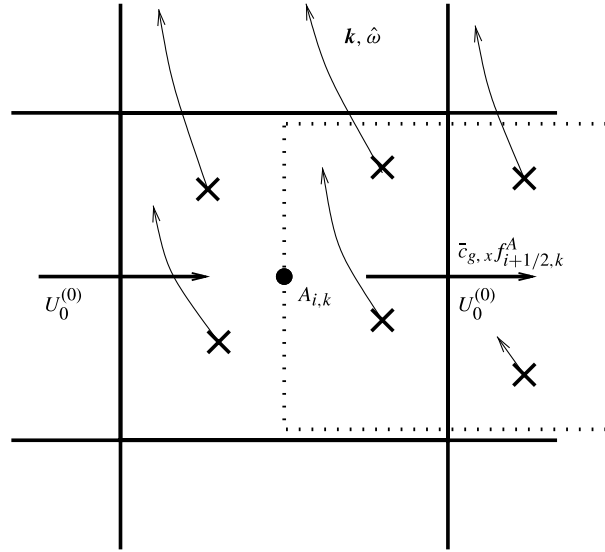
FIGURE 1. Finite-volume cell (solid line) for the conserved wave action A along with rays (crosses) carrying wave properties k, m, $\hat{\omega}$. All wave amplitudes are collocated with the wave action.

3.1. *Transport of rays and wave action*

In figure 1 a finite-volume cell (solid line) along with rays (crosses) is depicted. Note that the mean flow $\boldsymbol{U}_0^{(0)}$ is stored at the cell interfaces (C-grid). All wave amplitudes are cell centred: collocated with the wave action. In each Runge–Kutta stage the following procedure is carried out.

3.1.1. *Flux calculation*

Using the rays located in the dotted cell around edge $(i + 1/2)$, see figure 1, an average group velocity at the midpoint of this edge $\bar{c}_{gx,i+1/2}$ can be calculated. This velocity determines the upwind direction for the MUSCL upwind scheme:

$$f_{i+1/2} = \begin{cases} \bar{c}_{gx,i+1/2}A_{i+1/2}^- & \text{for } \bar{c}_{gx,i+1/2} > 0 \\ \bar{c}_{gx,i+1/2}A_{i+1/2}^+ & \text{for } \bar{c}_{gx,i+1/2} < 0. \end{cases} \tag{3.1}$$

The wave action $A_{i+1/2,k}$ at the cell interface $x_{i+1/2,k}$ is a second-order reconstructed value using a variant of the monotonized central-difference (MC) limiter described by Kemm (2010). Once all fluxes are calculated the wave action in each finite-volume cell can be updated:

$$\frac{\mathrm{d}}{\mathrm{d}t}A_i = -\frac{f_{i+1/2,k} - f_{i-1/2,k}}{\Delta x}. \tag{3.2}$$

The flux difference in the vertical direction has to be calculated and included analogously.

3.1.2. *Ray transport*

The rays are initially uniformly distributed over the mesh with wave numbers given by the test cases as described below. The number of rays per cell can be set via a parameter. Each ray carries the following information: Cartesian ray position $\boldsymbol{x} = (x, z)$,

wave vector $\boldsymbol{k} = (k, m)$, intrinsic group velocity $\boldsymbol{c}_g = (c_{gx}, c_{gz})$, intrinsic frequency $\hat{\omega}$, the position within the finite-volume grid $\boldsymbol{i} = (\mathrm{i}, k)$ as well as the position within a single finite-volume cell: upper/lower half and left/right half. In its present form the theory assumes that at each location there is just one local wave number and frequency. Dispersion, arising from initial configurations with different wave numbers, and thus group velocities, at the same location, are neglected.

For the ray transport we evolve in time

$$\frac{\mathrm{d}x}{\mathrm{d}t} = c_{gx} = \pm \frac{Nm}{k_T^3} m + U_0^{(0)} \tag{3.3}$$

$$\frac{\mathrm{d}z}{\mathrm{d}t} = c_{gz} = \pm \frac{Nm}{k_T^3} (-k) \tag{3.4}$$

where we use the branch with $c_{gx} > 0$ and $c_{gz} > 0$. In all test cases considered here the reference atmosphere is assumed to be isothermal at temperature T_{00}, so that the squared Brunt–Väisälä frequency is

$$N^2 = \frac{\kappa g^2}{R T_{00}} \tag{3.5}$$

with $\kappa = (\gamma - 1)/\gamma$ and $\gamma = c_p/c_v = 1.4$ being the adiabatic index for ideal gases and $k_T^2 = k^2 + m^2$ denotes the total wave number. The mean flow $\boldsymbol{u}^{(0)} = (U_0^{(0)}, 0)$ is defined at the cell edges (C-grid) and has to be interpolated to the rays appropriately.

After the ray displacement, their new position within the mesh, i.e. their corresponding cell indices, can be determined along with the change of the vertical wave number according to (2.24b). Rays leaving the domain are re-inserted at the opposite side of the mesh (periodic domain for rays) albeit with a re-initialization of the wave vector.

3.2. *Amplitude of first harmonic*

Once the wave action is known in a finite-volume cell, the buoyancy amplitude $B_1^{(1)}$ can be calculated using the relation

$$A = \frac{E'}{\bar{\hat{\omega}}} = \frac{1}{\bar{\hat{\omega}}} \frac{\rho^{(0)}}{2N^2} |B_1^{(1)}|^2 \tag{3.6}$$

where $\bar{\hat{\omega}}$ is the intrinsic frequency averaged over rays belonging to a finite-volume cell. All other wave 1 amplitudes $U_1^{(0)}, W_1^{(0)}, \Pi_1^{(2)}$ follow from the polarization relations (2.28) and are cell-centred, i.e. *collocated* with the wave action.

3.3. *Amplitude of second harmonic*

With the known amplitudes $U_1^{(0)}, W_1^{(0)}, B_1^{(1)}, \Pi_1^{(2)}$ of the first harmonic, we can calculate the amplitudes of the second harmonic $U_2^{(1)}, W_2^{(1)}, B_2^{(2)}, \Pi_2^{(3)}$ using the matrix equation (2.29). The system matrix $M_2 = M(2\hat{\omega}, 2k, 2m)$ can be inverted algebraically yielding

$$M_2^{-1} = D \left\{ \begin{array}{cccc} 2\mathrm{i}\bar{m}^2\bar{\hat{\omega}} & -2\mathrm{i}\bar{k}\bar{m}\bar{\hat{\omega}} & \bar{k}\bar{m}N & -\frac{1}{2}\mathrm{i}\bar{k}(4\bar{\hat{\omega}}^2 - N^2) \\ -2\mathrm{i}\bar{k}\bar{m}\bar{\hat{\omega}} & 2\mathrm{i}\bar{k}^2\bar{\omega} & -\bar{k}^2N & -2\mathrm{i}\bar{\hat{\omega}}^2\bar{m} \\ -\bar{k}\bar{m}N & \bar{k}^2N & 2\mathrm{i}\bar{\hat{\omega}}(\bar{m}^2 + \bar{k}^2) & -\bar{\hat{\omega}}\bar{m}N \\ -\frac{1}{2}\mathrm{i}\bar{k}(4\bar{\hat{\omega}}^2 - N^2) & -2\mathrm{i}\bar{\hat{\omega}}^2\bar{m} & \bar{\hat{\omega}}\bar{m}N & -\frac{1}{2}\mathrm{i}\bar{\hat{\omega}}(4\bar{\hat{\omega}}^2 - N^2) \end{array} \right\} \tag{3.7}$$

with

$$D = \frac{1}{4\bar{\hat{\omega}}^2 (\bar{m}^2 + \bar{k}^2) - \bar{k}^2 N^2}. \tag{3.8}$$

The equation can then be solved efficiently with a simple matrix multiplication. Since all wave amplitudes are cell centred, all rays within a cell have to be found and their wave properties have to be cell-averaged giving mean wave numbers $(\bar{k}, \bar{m})$ and mean intrinsic frequency $\bar{\hat{\omega}}$.

3.4. *Mean flow*

The RHS of the mean flow equations (2.36) and (2.35) is fully determined by the wave 1 amplitudes. For determining the mean flow the following procedure is helpful. Note that apart from $U_0^{(0)}$ the other mean flow quantities, $\Pi_0^{(2)}$ and $\Theta_0^{(2)}$, are not fully determined by the equation set: their x-mean values remain unknown and can be obtained by analysing higher-order terms of the WKB equations. Therefore, we restrict the analysis here to the x-derivatives $\partial \Pi_0^{(2)}/\partial x$ and $\partial \Theta_0^{(2)}/\partial x$.

3.4.1. *Mean velocity*

Taking the x-mean of (2.35) allows to calculate $\partial U_0^{(0)}/\partial t$ from the vertical gradient of the vertical gravity-wave momentum flux and, consequently, the change of the mean velocity $U_0^{(0)}$. The x-mean of the pressure term on the left-hand side disappears due to periodic boundary conditions (BCs) in the horizontal.

3.4.2. *Exner pressure*

Subtracting $\partial U_0^{(0)}/\partial t$ from (2.35) gives an equation for

$$\theta^{(0)} c_p \frac{\partial \Pi_0^{(2)}}{\partial x} = RHS(2.35) - \frac{\partial U_0^{(0)}}{\partial t}. \tag{3.9}$$

3.4.3. *Mean buoyancy*

Calculating the difference

$$\frac{\partial}{\partial z}\left(\frac{(2.35)}{\theta^{(0)}}\right) - \frac{\partial}{\partial x}\left(\frac{(2.36)}{\theta^{(0)}}\right) \tag{3.10}$$

we obtain the following equation for $\partial \Theta_0^{(2)}/\partial x$

$$\frac{\partial}{\partial z}\left(\frac{1}{\theta^{(0)}}\frac{\partial U_0^{(0)}}{\partial t}\right) + \frac{\partial}{\partial x}\left(g\frac{\Theta_0^{(2)}}{\theta^{(0)2}}\right) - \frac{\partial}{\partial x}\left(g\frac{|\Theta_1^{(1)}|^2}{2\theta^{(0)3}}\right)$$
$$= \frac{\partial}{\partial z}\left(\frac{RHS(2.35)}{\theta^{(0)}}\right) - \frac{\partial}{\partial x}\left(\frac{RHS(2.36)}{\theta^{(0)}}\right). \tag{3.11}$$

4. Validation part I: one-dimensional GWP

In the following section we compare the propagation of a GWP once calculated with a full model of the pseudo-incompressible equations and once with the ray tracer integrating the WKB equations as described in §3. For the full model we use a three-dimensional finite-volume model of the pseudo-incompressible equations (pincFloit) described by Rieper, Hickel & Achatz (2013). For the spatial discretization we use a second-order MUSCL scheme with the MC limiter. The third-order low-storage Runge–Kutta scheme by Williamson (see Durran 1999) is used for advancing

the equations in time. At first we analyse a one-dimensional GWP with a Gaussian profile only along the vertical axis since the Fourier analysis along the x-axis is then straightforward and the insight we get can later be used for the more complex two-dimensional case presented in § 5.

4.1. *Description of the reference test case*

First we present numerical results for a reference test case; later we show the influence of some parameters on the validity of the WKB theory. In the isothermal reference state with $T_{00} = 300$ K a wave packet is initialized with the buoyancy amplitude

$$\hat{b}(z) = a\frac{N^2}{m} \exp\left[-\frac{(z - z_{Center})^2}{2\sigma^2}\right] \tag{4.1}$$

with the amplitude $a = 0.1$, which corresponds to 10 % of the threshold of static instability, the isothermal Brunt–Väisälä frequency for $T_{00} = 300$ K of $N = 0.018$ s^{-1}, the half-width $\sigma = 5$ km and the centre of the wave packet at $z_{Center} = 30$ km. Note that in this configuration the distinguished limit of multiple-scale asymptotics is already undergoing a critical test since the isothermal potential-temperature scale height g/N^2 is considerably larger than the wave-packet half-width σ. Using the polarization relations we set the following initial fields

$$u_{t=0} = \frac{m}{k}\frac{\hat{\omega}}{N^2}\hat{b}\cos\left(kx + mz - \frac{\pi}{2}\right) \tag{4.2}$$

$$w_{t=0} = \frac{\hat{\omega}}{N^2}\hat{b}\cos\left(kx + mz + \frac{\pi}{2}\right) \tag{4.3}$$

$$b_{t=0} = \hat{b}\cos(kx + mz) \tag{4.4}$$

$$\pi_{t=0} = \frac{m}{k^2}\frac{\hat{\omega}^2}{N^2}\frac{1}{c_p\theta^{(0)}(z)}\hat{b}\cos\left(kx + mz - \frac{\pi}{2}\right). \tag{4.5}$$

For the wavelengths we set $\lambda_x = \lambda_z = 1$ km. The domain of the full model has the size $(l_x, l_z) = (1$ km, 60 km$)$ at a resolution of $n_x \times n_z = 64 \times 3840$ while the ray tracer runs at a resolution of $n_x \times n_z = 1 \times 1000$ (which is far more than actually needed but keeping us on the safe side). The buoyancy field is transformed into a density perturbation.

In the remainder of this section we will only discuss the gravity wave and its higher harmonics. The mean flow behaves very much as in the two-dimensional case where it will be given due attention.

4.2. *Validation of the reference test case*

4.2.1. *Harmonics 1, 2 and higher*

In figure 2 Hovmöller diagrams, i.e. z–t contour plots, of the buoyancy for the first harmonic $B_1^{(1)}$ (a,b), the second harmonic $B_2^{(2)}$ (c,d) and the third harmonic $B_3^{(2)}$ (e,f) calculated with the full model (a,c,e) and the WKB model (b,d,e) is shown. There is a perfect agreement for wave 1. Wave 2 is by a factor of 10^3 smaller than wave 1 which is of about of the same order as the scale-separation ratio $\varepsilon = (\lambda_z/2\pi)/(g/N^2)$. The agreement between full and WKB model is still very good but we can make out a weak 'pumping' of the amplitude obtained with the full model. The third harmonic (lower row) should be absent according to the WKB theory or, to be more precise, should be of a smaller order in ε. This means that if we took smaller terms into account we might be able to show that $B_3^{(3)} \neq 0$. And, indeed, the full model shows a
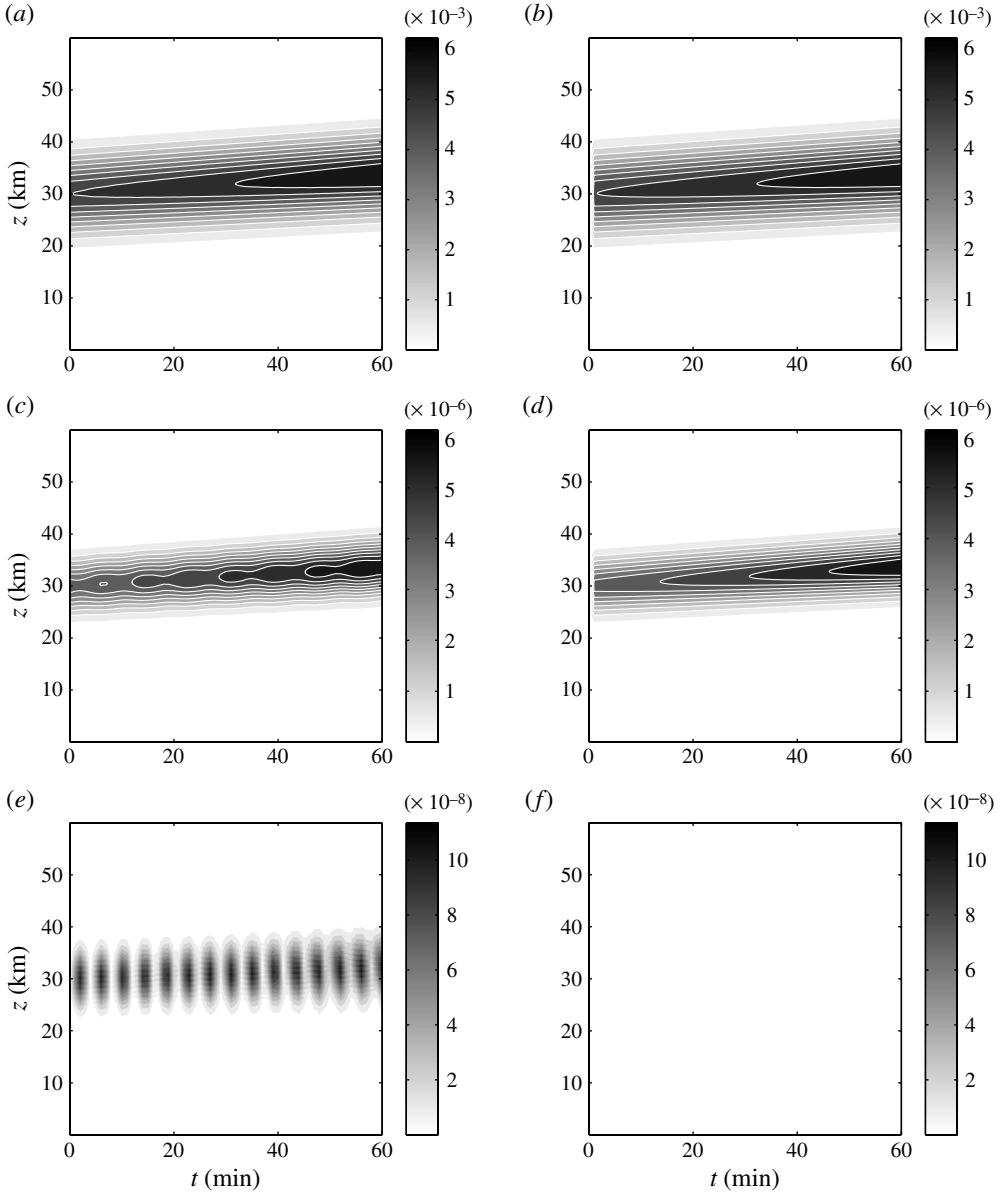
FIGURE 2. For the one-dimensional case in the standard setting (see the main text) and $a = 0.1$: Hovmöller diagrams of buoyancy for the first harmonic $B_1^{(1)}$ (*a,b*), the second harmonic $B_2^{(2)}$ (*c,d*) and the third harmonic $B_3^{(2)}$ (*e,f*) calculated with the full model (*a,c,e*) and the WKB model (*b,d,f*). The isolines in the top range from 5.7×10^{-4} to 5.7×10^{-3} in steps of 5.7×10^{-4}, in the middle from 5.7×10^{-7} to 5.7×10^{-6} in steps of 5.7×10^{-7} and in the bottom from 1.0×10^{-8} to 1.0×10^{-7} in steps of 1.0×10^{-8}. Units are m s^{-2}. The small parameters defined in the main text are $(\varepsilon, \varepsilon_1, \varepsilon_2) = (5.2 \times 10^{-3}, 5.2 \times 10^{-4}, 3.2 \times 10^{-2})$.

very weak amplitude, which is again by a factor of 10^2 smaller than wave 2 and which also shows this pumping behaviour. This effect becomes more evident in figure 3, where the line pair in the middle annotated with $\lambda = 1000$ m represents the reference
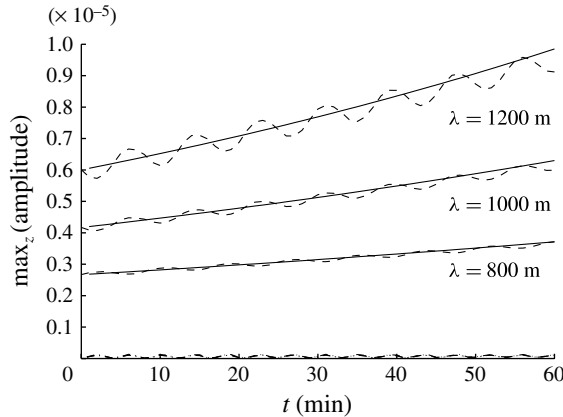
FIGURE 3. As figure 2, but now the influence of wavelength on amplitude maxima along z plotted against time for waves 2 and 3: —— , wave 2 with WKB; ––, wave 2 with the full model; –·–, wave 3 with the full model. Shown are the test cases with $\lambda = 800$ m and $(\varepsilon, \varepsilon_2) = (4.1 \times 10^{-3}, 2.5 \times 10^{-2})$ (bottom), $\lambda = 1000$ m and $(\varepsilon, \varepsilon_2) = (5.2 \times 10^{-3}, 3.2 \times 10^{-2})$ (middle), and $\lambda = 1200$ m and $(\varepsilon, \varepsilon_2) = (6.2 \times 10^{-3}, 3.8 \times 10^{-2})$ (top). In all cases $\varepsilon_1 = 0.1\varepsilon$.

test case. In the figure the amplitude maxima taken along the z-axis, i.e. the peak of the Gaussian, are plotted against time. Note that all higher wave numbers (not shown) are also present in the full model solution and have the same order of magnitude as wave 3. The pumping frequency and amplitude is not predicted by the WKB theory and will be analysed in the following parameter study.

4.3. *Parameter study*

The theory to be validated here has been obtained as a distinguished limit within multiple-scale asymptotics. The governing small parameter is the scale-separation ratio

$$\varepsilon = \frac{L}{H_\theta} = \frac{N^2}{2\pi g}\lambda_z \tag{4.6}$$

between the inverse wave number of the gravity wave and potential-temperature scale height. Based on linear theory, it is assumed to be of the same order as the ratio between the leading-order amplitude of the gravity-wave potential-temperature fluctuations and the reference-state potential temperature,

$$\varepsilon_1 = \frac{\Theta_1^{(1)}}{\theta^{(0)}} = \frac{B_1^{(1)}}{g}. \tag{4.7}$$

Up to the Gaussian envelope the gravity-wave buoyancy amplitude is $\hat{b} = aN^2/m$, leading to

$$\varepsilon_1 = a\frac{N^2}{2\pi g}\lambda_z. \tag{4.8}$$

The assumptions of the distinguished limit are met as long as $a = O(1)$. The limit case $a = 1$, however, immediately leads to a turbulent wave breakdown so that we can only assume a is somewhat less than 1. But, strictly speaking, a being asymptotically small would be a situation that requires testing. Finally, it was also assumed that gravity-

wave amplitudes have the same spatial scale as the reference-atmosphere potential temperature so that the scale-separation ratio

$$\varepsilon_2 = \frac{\lambda_z}{2\pi\sigma} \tag{4.9}$$

should be $O(\varepsilon)$. As mentioned above, the test case discussed so far does not strictly meet this condition, yet the theory works well for it. A parameter study within which the three ε are varied relative to each other thus seems to be in place. The analysis below, accompanied by an investigation of the influence of the numerics, addresses this, along with two other questions: first, what influences the amplitude of wave 3 and higher, which should vanish in the present WKB theory up to first order in ε and, second, what influences the 'pumping' of the wave 2 amplitude? For testing the validity of the WKB theory we varied the wavelength and the amplitude of the initial wave packet. In the following we present the major results. In all of the cases that are presented, wave 1 agrees perfectly between the full and WKB models, thus we do not always show it.

4.3.1. *Influence of numerics*

It is quite interesting to see how the full-model numerics influences the deviation from the WKB predictions. Here we simply state the results, which are discussed in Rieper *et al.* (2013) with a focus on the numerics used in the pseudo-incompressible, finite-volume model *pincFloit*. A major aspect is the *spatial resolution*, given by the number of cells per wave 1 wavelength n_λ. We found that with $n_\lambda = 16$ the amplitudes of waves 3 and 5 are of the same order of magnitude as wave 2. With $n_\lambda = 32$, waves 3 and 5 are distinctly smaller than wave 2 but only for $n_\lambda \geqslant 64$ do the higher harmonics practically vanish as predicted by WKB theory. Note that the choice of the spatial discretization (flux function and limiter) also influences the deviations, especially in the higher harmonics.

4.3.2. *Influence of wavelength*

For an analysis of the impact of the scale-separation parameter as such, we have varied the wavelength and kept all other parameters constant, thus also keeping the ratios above constant. We varied the wavelength $\lambda_x = \lambda_z = \lambda$ around the reference test case

$$\lambda = 800 \text{ m}/1000 \text{ m}/1200 \text{ m} \tag{4.10}$$

while keeping a constant size of the wave packet. The resolution was kept at $n_x \times n_z = 64 \times 3840$ and only the horizontal domain size was adapted to the wavelength, i.e. $l_x = 800 \text{ m}/1000 \text{ m}/1200 \text{ m}$. In figure 3 the amplitude maxima along the z-axis are plotted against time for all three wavelengths. Shown are wave 2 for the WKB model (solid lines) and the full model (dashed lines) along with the wave 3 amplitude of the full model (dash-dotted lines). For all parameters the WKB theory predicts the correct mean of wave 2. The wave 2 amplitude mean gets somewhat below the WKB wave 2 mean after some time. This can be attributed to the numerical damping of the full model taking into account that 60 min physical time need some 3600 time steps of calculation in the full model. The pumping of the wave 2 amplitude increases with larger λ, i.e. with larger ε. For all parameters the wave 3 amplitude is of comparable size. Thus, we can say as $\varepsilon \to 0$ the pumping disappears and the WKB theory predictions are very well matched. For larger ε only the mean amplitude is still correctly predicted and the pumping is beyond the WKB theory.
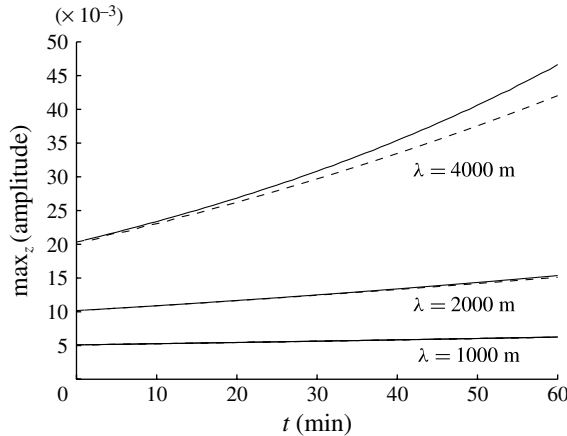
FIGURE 4. As figure 2, but now the influence of wavelength on amplitude maxima along z plotted against time for wave 1: —, wave 1 with WKB; – –, wave 1 with full model. Shown are the test cases with $\lambda = 1000$ m and $(\varepsilon, \varepsilon_2) = (5.2 \times 10^{-3}, 3.2 \times 10^{-2})$ (bottom), $\lambda = 2000$ m and $(\varepsilon, \varepsilon_2) = (1.0 \times 10^{-2}, 6.4 \times 10^{-2})$ (middle) and $\lambda = 4000$ m and $(\varepsilon, \varepsilon_2) = (2.0 \times 10^{-2}, 0.13)$ (top). In all cases $\varepsilon_1 = 0.1\varepsilon$.

At even larger wavelength, increasing up to $\lambda = 4000$ m, at least the wave 1 amplitude is well-matched, as can be seen in figure 4. Owing to the definition of buoyancy amplitude via the normalized amplitude

$$\hat{b} = a\frac{N^2}{m} \tag{4.11}$$

the signal amplitude varies with changing λ_z. The larger the wavelengths, however, the more the full-model amplitude falls behind the WKB predicted amplitude. Part of this could be due to wave dispersion, the more relevant the closer gravity-wave wavelength and the spatial scale of the envelope become, but they are not included in the present XWKB. A similar result was obtained for waves 2 and 3 as depicted in figure 5. Wave 2 shows two kinds of deviations from the WKB predictions: an increasing oscillatory behaviour and, as for wave 1, a fall back of mean-amplitude behind the WKB predicted amplitude. Note, however, that even under these conditions XWKB still performs quite well, even quantitatively.

4.3.3. *Influence of amplitude*

As the non-dimensional wave amplitude a is increased, two counteracting effects compete with each other. On the one hand, the ratios ε_1 and ε are approaching each other and, as long as we remain below the threshold for turbulent breaking, the assumptions of the distinguished limit are met better. On the other hand, as a is increased, nonlinear gravity-wave instabilities gain in relevance (e.g. Lombard & Riley 1996; Achatz 2005), which are not described by the present theory. We first note that below the threshold for breaking, the wave 1 amplitude is always in good agreement with the theory (not shown). Wave 2, however, deteriorates in quality as a is increased. If the amplitude a is varied from $a = 0.1$ via $a = 0.25$ to $a = 0.5$ while keeping all other quantities as in the reference case, we obtain the result shown in figure 6 with the same line coding as in the λ study. The (initial) wave 2 amplitude increases by a factor of roughly 5. For smaller amplitudes a, i.e. smaller ε_1, the pumping decreases
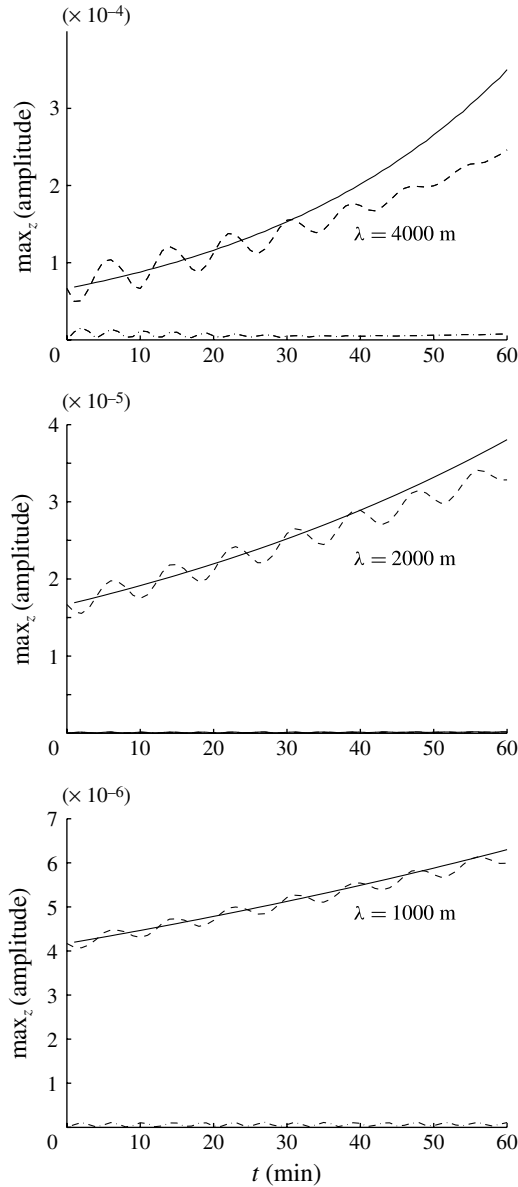
FIGURE 5. As figure 4, but now for waves 2 and 3.

and the WKB predictions are better met as we would expect for $\varepsilon_1 \to 0$. It thus appears that the discrepancy between ε and ε_1 matters less than a being large. Note, however, that part of the relative decay in wave 2 amplitude at large a is due to numerical damping which increases in the presence of steeper gradients. Note also that the breaking of the wave sets in at $t \approx 40$ min for initial $a = 0.75$, to be expected already below an instantaneous $a = 1$ (Fritts *et al.* 2006; Achatz 2007), leading to an exponential amplitude growth for all wave numbers represented on the grid as can be seen in figure 7. Still, however, up to the point of breaking the predictions from XWKB are quite reliable.
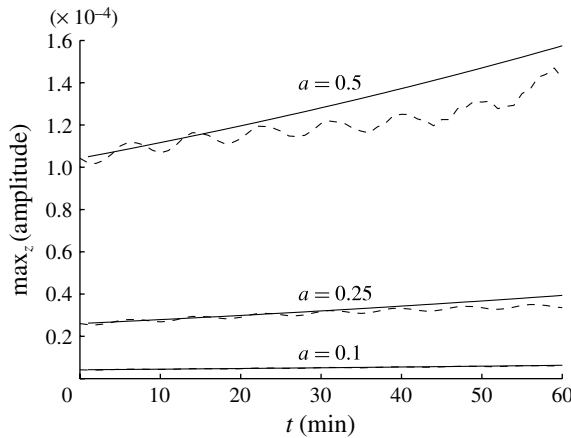
FIGURE 6. As figure 2, but now the influence of normalized initial amplitude a on the amplitude maxima along z plotted against time for wave 2: —, wave 2 with WKB; – –, wave 2 with the full model. Shown are the test cases with $a = 0.1$ and $\varepsilon_1 = 2.6 \times 10^{-3}$ (bottom), $a = 0.25$ and $\varepsilon_1 = 1.3 \times 10^{-3}$ (middle) and $a = 0.5$ and $\varepsilon_1 = 5.2 \times 10^{-4}$ (top). In all cases $(\varepsilon, \varepsilon_2) = (5.2 \times 10^{-3}, 3.2 \times 10^{-2})$.
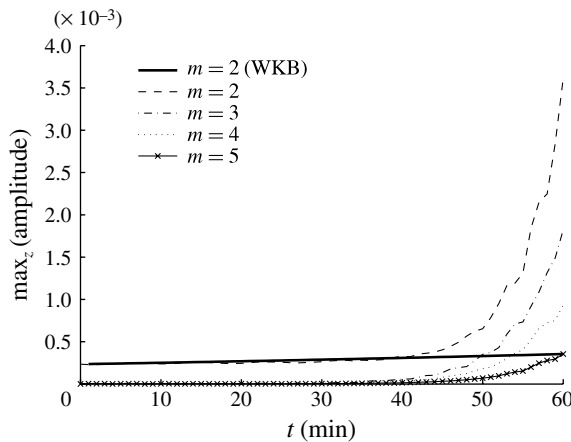

FIGURE 7. As figure 2, but now the long time behaviour of the buoyancy amplitude b plotted against time for waves 2–5 with an initial amplitude $a = 0.75$. The various small parameters are $(\varepsilon, \varepsilon_1, \varepsilon_2) = (5.2 \times 10^{-3}, 3.9 \times 10^{-3}, 3.2 \times 10^{-2})$.

4.4. *Wave–mean-flow interaction in long integrations*

One might apprehend that in the analyses above XWKB is not really tested up to its limits since in the short integrations considered, nonlinear interactions between the GWP and mean flow do not have enough time to develop. We therefore consider here two additional cases where this interaction can become more pronounced. In the first case we launch the wave packet at a low initial amplitude $a = 0.1$ and let it propagate upwards until nonlinear dissipation sets in. In the second case a hydrostatic wave packet is launched below a horizontal wind jet which is able to modify the wave-packet properties. Throughout these two test cases we use a cosine bell-shaped
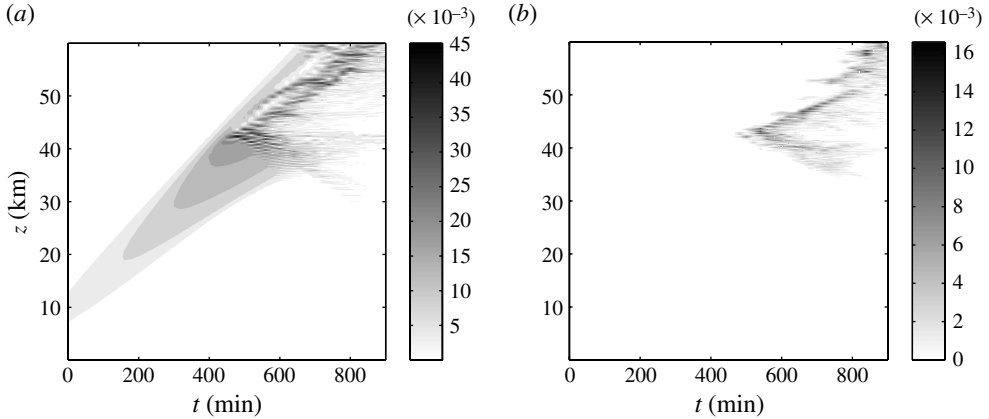
FIGURE 8. For the one-dimensional-case of a non-hydrostatic GWP with initial amplitude $a = 0.1$ launched in the pseudo-incompressible equation code at altitude $z = 10$ km: Hovmöller diagrams of buoyancy for the first harmonic $B_1^{(1)}$ (*a*) and the second harmonic $B_2^{(2)}$ (*b*). Units are m s^{-2}. The small parameters defined in the main text are $(\varepsilon, \varepsilon_1, \varepsilon_2) = (5.2 \times 10^{-3}, 5.2 \times 10^{-4}, 3.2 \times 10^{-2})$. Horizontal and initial vertical wavelength are $\lambda_x = \lambda_z = 1$ km.

amplitude

$$\hat{b}(z) = \frac{1}{2} \frac{aN^2}{m} \left[1 + \cos\left(\frac{\pi(z - z_{Center})}{\sigma} \right) \right] \tag{4.12}$$

for $|z - z_{Center}| < \sigma$ and $\hat{b}(z) = 0$ elsewhere with a half-width of $\sigma = 10$ km.

4.4.1. *Uniform background*

Figure 8 shows the time development, from the pseudo-incompressible equation code, of the first and second harmonic of the GWP launched with initial amplitude $a = 0.1$ at altitude $z = 10$ km. Horizontal and vertical wavelength are $\lambda_x = \lambda_z = 1$ km. After 400 min strongly nonlinear behaviour sets in. The amplitude with respect to static instability immediately before this collapse is below $a = 0.4$. Direct static instability can thus be excluded as a destabilizing mechanism. As is shown below, the local vertical wavelength grows in the vertical propagation, in response to gradients in the wave-induced mean flow. It thus becomes larger than the horizontal wavelength. It is known that under such conditions modulational instability (Sutherland 2006; Dosser & Sutherland 2011) can lead to enhanced local gravity-wave amplitude growth. We speculate that this leads indirectly to local amplitudes large enough for static instability. Indeed, right after the onset of wave dissipation total potential temperature develops negative vertical gradients in many places (not shown).

The XWKB code collapses when the nonlinear dissipation sets in. We assume that this is related to the fact that at this point the central assumption of just one wavelength at a given location is no longer fulfilled. Corresponding extensions will have to be considered in the future. Up to the point of destabilization, however, the XWKB predictions work quite well. To demonstrate this we compare the predictions of the XWKB code with those from the pseudo-incompressible equation code for
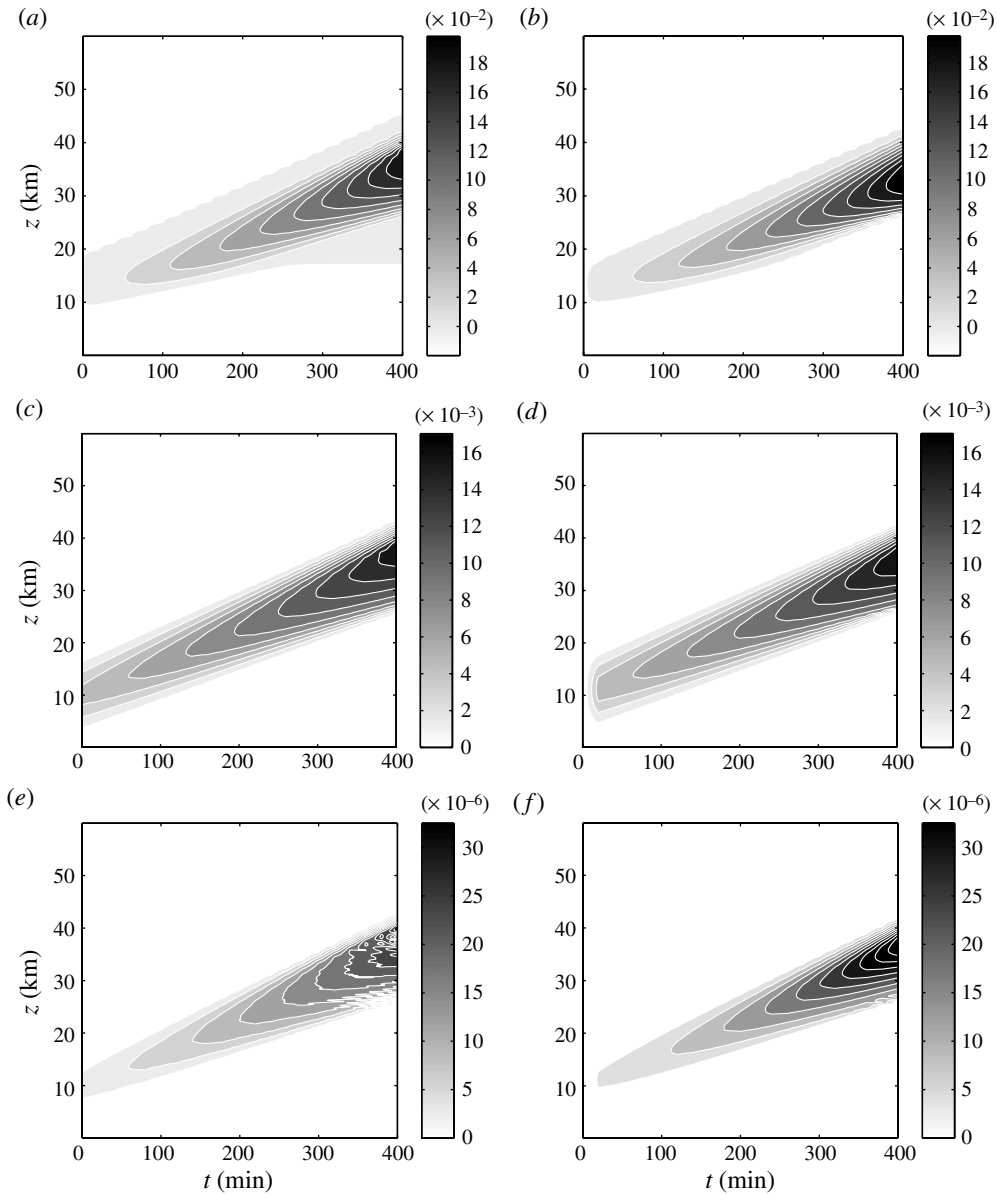
FIGURE 9. As figure 8, but now comparing, up to the onset of nonlinear dissipation, the predictions from the pseudo-incompressible equation code (a,c,e) and the XWKB code (b,d,f). Shown are the mean horizontal wind $U_0^{(0)}$ (a,b, units m s^{-1}), the first harmonic of buoyancy $B_1^{(1)}$ (c,d, units m s^{-2}) and the second-harmonic buoyancy $B_2^{(2)}$ (e,f, units m s^{-2}).

the mean horizontal wind and the first- and second-harmonic buoyancy amplitudes in figure 9. The mean horizontal wind has also been compared to the prediction

$$U_0^{(0)} = -\frac{1}{2\rho^{(0)}} \mathrm{Re}\,(\zeta \xi^*) \qquad (4.13)$$
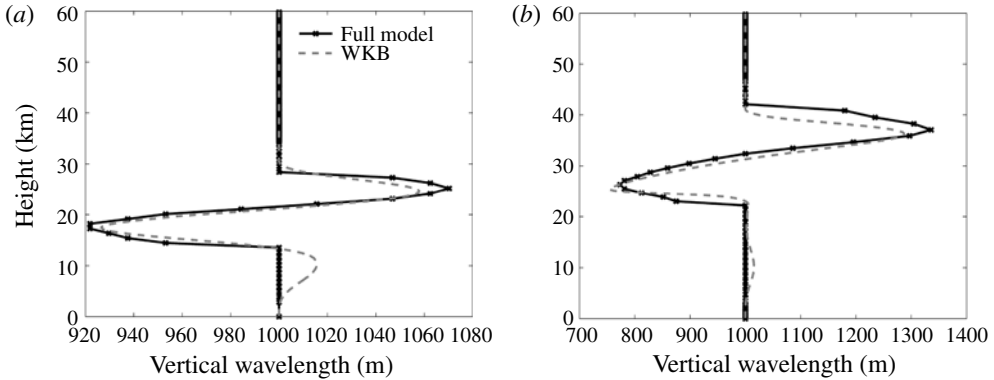
FIGURE 10. For the same case as shown in figures 8 and 9 the local vertical wavelength, as predicted by the pseudo-incompressible equation code and the XWKB code for $t = 180$ min (*a*) and $t = 360$ min (*b*).

from (2.40) and (2.41). Above the region of the wave-packet initialization the agreement is very good (not shown). Similarly good agreement is also visible in figure 10 where the predictions for the local vertical wavelength are compared with each other. Next to the good agreement also the growth of the wavelength in the upper part of the GWP is of interest. As argued above, this might cause the final GWP destabilization. Indeed at $t = 360$ min the instability criterion given by Sutherland (2006), i.e. $\lambda_x/\lambda_z \leqslant 0.7$ is already nearly fulfilled.

4.4.2. *Wave-packet propagation through a horizontal-wind jet*

In all cases considered above the initial mean horizontal wind was zero. Wave–mean-flow interaction there implied first the generation of a wave-induced mean flow which then can also influence the GWP. That latter process is facilitated from the start in a case considered here, where a hydrostatic wave packet with horizontal and initial vertical wavelengths $(\lambda_x, \lambda_z) = (10, 1)$ km is initialized below a horizontal-wind jet of the shape

$$U_0^{(0)} = \begin{cases} \dfrac{U_0}{2} \left\{ 1 + \cos\left[\dfrac{\pi}{\Delta L} (z - z_0) \right] \right\} & |z - z_0| \leqslant \Delta L \\ 0 & \text{otherwise.} \end{cases} \tag{4.14}$$

The jet is located at $z_0 = 25$ km and has a half-width $\Delta L = 5$ km. The initial GWP is at altitude 10 km, with a half-width $\sigma = 5$ km. To avoid an initial wave–mean-flow interaction the GWP amplitude has been given the same cosine profile as the jet, with zero amplitude outside of $|z - z_{Center}| \leqslant \sigma$. The initial amplitude of the GWP is $a = 0.1$. Its horizontal phase and group velocities are negative so that no critical layer exists. According to WKB theory reflection of the GWP would be possible, however, if the jet were strong enough so that the GWP vertical wavelength becomes infinite in the course of the upward propagation through the jet (e.g. Sutherland 2010). In a steady horizontal mean flow, assumed in this discussion for simplicity, frequency is conserved along a ray, while its horizontal homogeneity implies conserved horizontal wave number k. The vertical wave number must adjust, however, in the course of the GWP propagation in order keep the frequency $\omega = U_0^{(0)} k - Nk/\sqrt{1 + (m/k)^2}$ constant. This causes the vertical wavelength to grow. Reflection would be observed if m could

pass through zero. This would happen if

$$U_0 \geqslant \frac{N}{k} \left(1 - \frac{1}{\sqrt{1 + \frac{m_0^2}{k^2}}} \right) \tag{4.15}$$

where m_0 is the initial vertical wave number. For the GWP here this would imply $U_0 \geqslant 25.8 \text{ m s}^{-1}$. In this situation our XWKB code would have to break down since it cannot handle a situation where at a single location reflected rays exist which have a different vertical wave number sign than the approaching rays. We have therefore chosen a weak-jet case with $U_0 = 5 \text{ m s}^{-1}$. Jets with peak values 10 and 20 m s^{-1} have also been considered. There, however, the XWKB code was found to be unstable, probably due to crossing rays in the nonlinear development which mean wind and GWP take in the later phases of these cases. For the weak-jet case, however, XWKB can give useful predictions. Figure 11 compares the prediction for the mean-horizontal-wind deviation from the initial jet, the first-harmonic buoyancy amplitude and the second-harmonic buoyancy amplitude, as obtained from the two codes. Figure 12 compares the predictions for the vertical wavelength. While some differences are visible in the last phase of the simulations, at least qualitative agreement can be diagnosed over the whole time span.

5. Validation part II: two-dimensional GWP

The two-dimensional case is more interesting because it is more general but also more challenging, for two reasons: first, to obtain the same resolution of the wave as in the one-dimensional case, i.e. $n_\lambda = 64$ points per wave 1 length, we would need a two-dimensional resolution of $n_x \times n_z \geqslant 2500^2$, which makes runs on a single processor very time-consuming; second, the signal has, both in x and z, a Gaussian profile and a Fourier transform can no longer be used to separate the wave components in the wave packet. The signals we are looking for, the wave 2 and wave 3 amplitude, are by a factor of at least 1000 smaller than the wave 1 signal and any manipulation of the data can affect this weak signal. After presenting the test case we show the wave 1, wave 2 and wave 3 amplitudes, as for the one-dimensional case, and then present the results for the mean flow and the difference between pseudo-incompressible and anelastic WKB theory.

5.1. *Description of the test case*

The two-dimensional wave packet is initialized with the buoyancy amplitude

$$\hat{b}(x, z) = a \frac{N^2}{m} \exp\left[-\frac{(x - x_{Center})^2 + (z - z_{Center})^2}{2\sigma^2} \right] \tag{5.1}$$

where we use the same quantities as for the one-dimensional test case with some modifications: $\sigma = \sigma_x = \sigma_z = 5$ km, the domain was made smaller to decrease computing times to $(l_x, l_z) = (40 \text{ km}, 40 \text{ km})$ at a full-model resolution of $n_x \times n_z = 1280 \times 1280$ and a ray-tracer resolution of $n_x \times n_z = 100 \times 100$. The full-model resolution resolves the wave 1 with $n_\lambda = 32$ points, i.e. a factor of 2 lower than in the one-dimensional case. We reduced the physical time of the test run to $t_{max} = 20$ min in order to avoid the wave packet interfering with the boundary, since the domain was made more compact to save computing time.
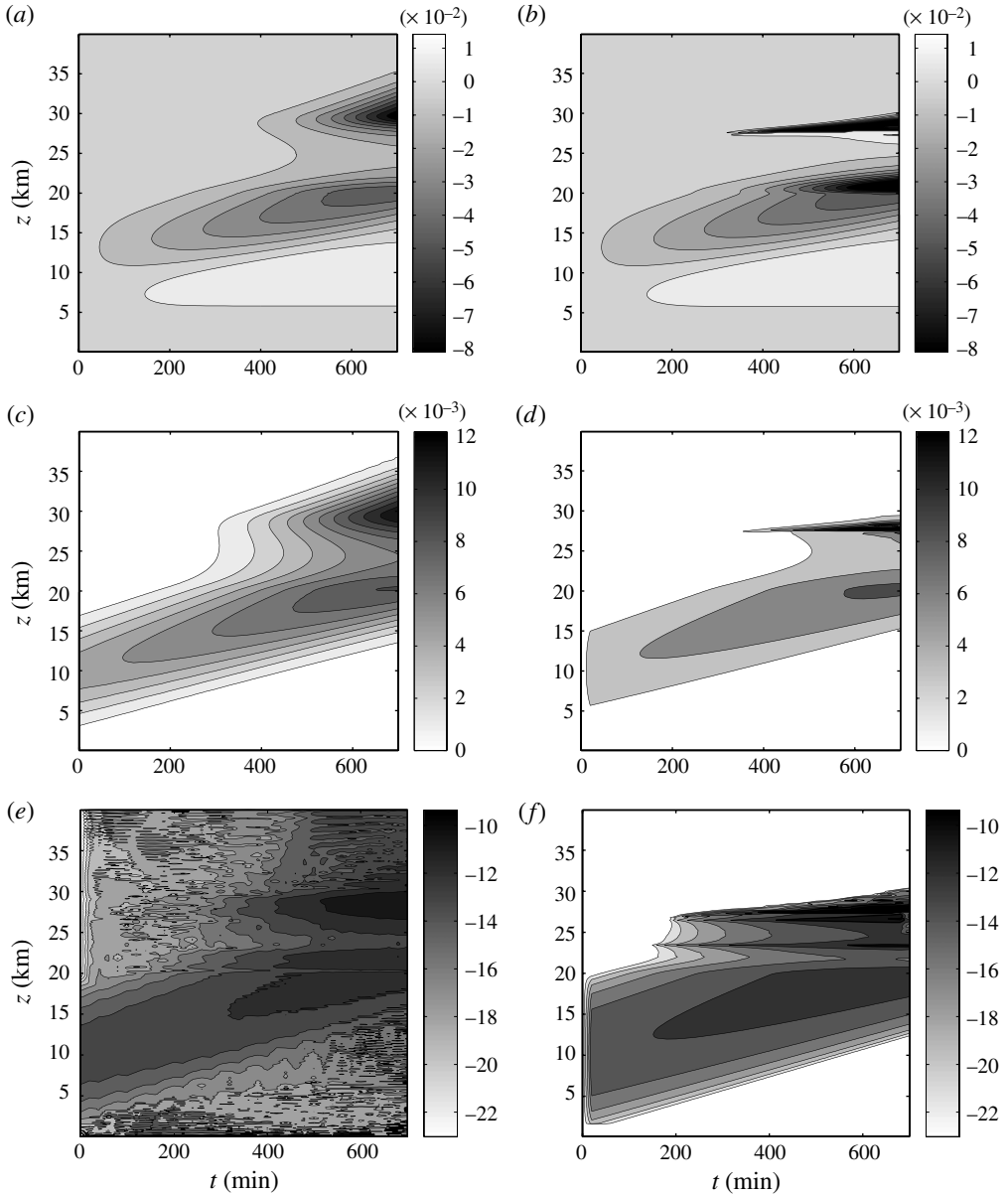
FIGURE 11. The one-dimensional case of a hydrostatic GWP with initial amplitude $a = 0.1$ launched at altitude $z = 10$ km below a horizontal wind jet at altitude 25 km: Hovmöller diagrams of the predictions from the pseudo-incompressible equation code (*a,c,e*) and the XWKB code (*b,d,f*). Shown are the deviation of the mean horizontal wind $U_0^{(0)}$ from the jet (*a,b*, units m s^{-1}), the first-harmonic buoyancy amplitude $B_1^{(1)}$ (*c,d*, units m s^{-2}) and the second-harmonic buoyancy amplitude $B_2^{(2)}$ (*e,f*, units m s^{-2}). For better visibility the logarithm of the second-harmonic buoyancy amplitude is shown. Horizontal and initial vertical wavelengths are $(\lambda_x, \lambda_z) = (10, 1)$ km. The small parameters defined in the main text are $(\varepsilon, \varepsilon_1, \varepsilon_2) = (5.2 \times 10^{-3}, 5.2 \times 10^{-4}, 3.2 \times 10^{-2})$.
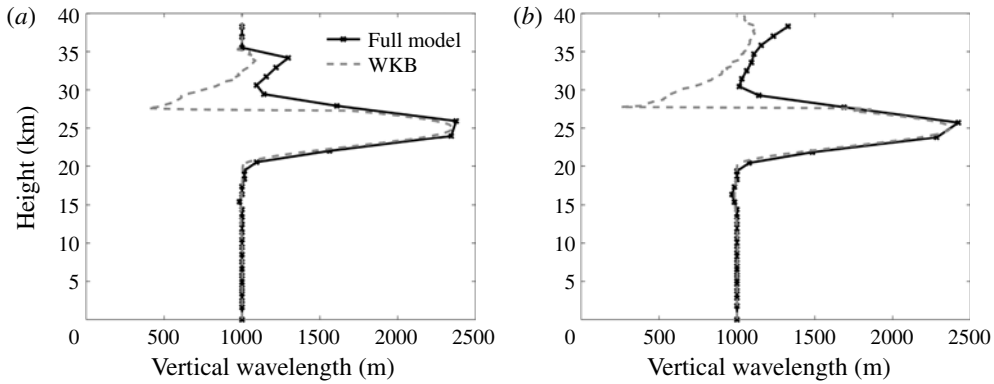
FIGURE 12. For the same case as shown in figure 11, the local vertical wavelength, as predicted by the pseudo-incompressible equation code and the XWKB code $t = 360$ min (a) and $t = 540$ min (b).

5.2. *Harmonics 1, 2 and 3*

In figure 13 the results of the two-dimensional test cases are shown in Hovmöller diagrams of the buoyancy at the horizontal location of largest wave amplitude, with full-model results on figure 13(a,c,e) and WKB-model results on figure 13(b,d,f). The data processing by which we have obtained the spatially dependent wave amplitudes is discussed in the Appendix. In the upper row the amplitude of wave 1 is in very good agreement. The full model produces an oscillating second harmonic (middle row), while WKB predicts a continuously increasing amplitude. Nevertheless, the amplitude-mean obtained with the full model agrees well with the amplitude predicted by WKB as can be seen in figure 14. Wave 3 (bottom row of figure 13) and all higher wave numbers (not shown) are slightly weaker than wave 2 and should be at the most first order in ε according to WKB theory. Recall that in this test case the resolution is only half as good as in the one-dimensional case and it is therefore sensible that the WKB predictions are not as well met. In addition, it cannot be guaranteed that in the extraction process of waves 2 and 3 the signal is not affected.

5.3. *Mean flow*

To calculate the mean flow variables $U_0^{(0)}$, $B_0^{(2)}$ and $\Pi_0^{(2)}$ for the WKB theory we follow the steps given in § 3.4. For the full-model data we apply a filter along x and z with the filter size corresponding to the wave 1 length

$$\overline{f_{i_0}}^x = \sum_{i=i_0-(n_\lambda/2)}^{i_0+(n_\lambda/2)-1} f_i \tag{5.2}$$

$$\overline{f_{i_0}}^{x,z} = \sum_{k=k_0-(n_\lambda/2)}^{k_0+(n_\lambda/2/2)-1} f_k. \tag{5.3}$$

This procedure was applied twice to get rid of all oscillations in the solution. Figure 15 shows the mean horizontal velocity in the full model at a very early (5 min) and a somewhat later (20 min) instance of the development. Note how quickly the flow adjusts to the horizontally homogeneous state predicted by (2.34), following
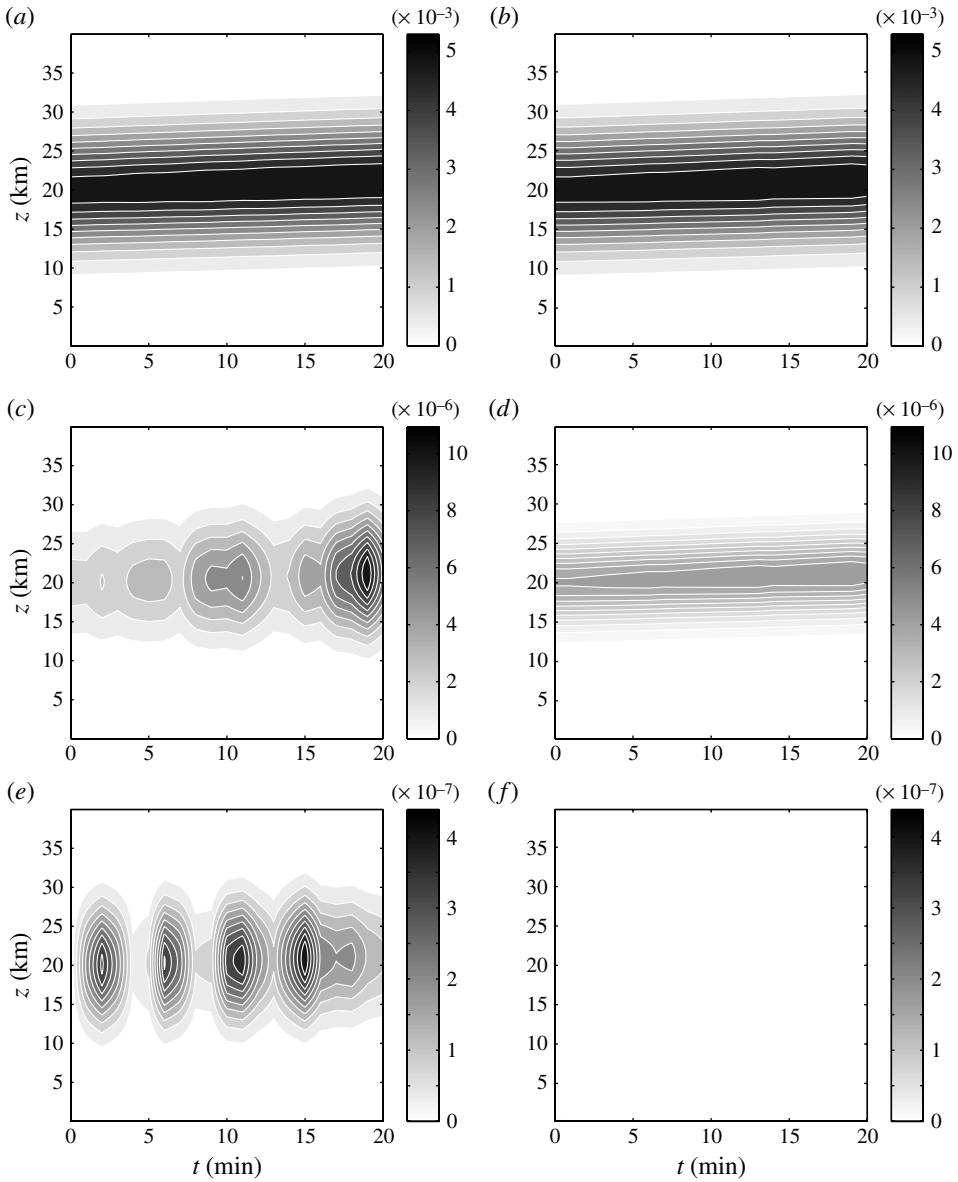
FIGURE 13. For the two-dimensional case in the standard setting (see the main text): Hovmöller diagrams of buoyancy for the first harmonic $B_1^{(1)}$ (a,b), the second harmonic $B_2^{(2)}$ (c,d) and the third harmonic $B_3^{(2)}$ (e,f) calculated with the full model (a,c,e) and the WKB model (b,d,f). The isolines in the (a,b) range from 5×10^{-4} to 5×10^{-3} in steps of 5×10^{-4}; in (c,d) from 4.2×10^{-7} to 4.2×10^{-6} in steps of 4.2×10^{-7} and in (e,f) diagram from 4.2×10^{-8} to 4.2×10^{-7} in steps of 4.2×10^{-8}. Units are m s^{-2}. The various small parameters are $(\varepsilon, \varepsilon_1, \varepsilon_2) = (5.2 \times 10^{-3}, 5.2 \times 10^{-4}, 3.2 \times 10^{-2})$.

from the weakness of the vertical wind and the non-divergence constraint. In figure 16 the results obtained with the full model (a,c,e) are compared with the WKB theory predictions (b,d,f).
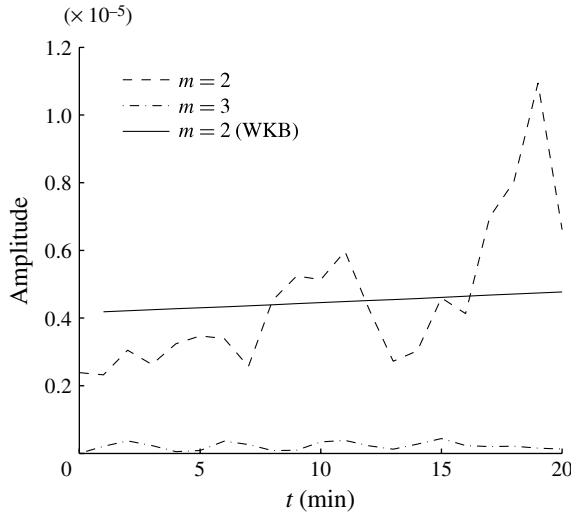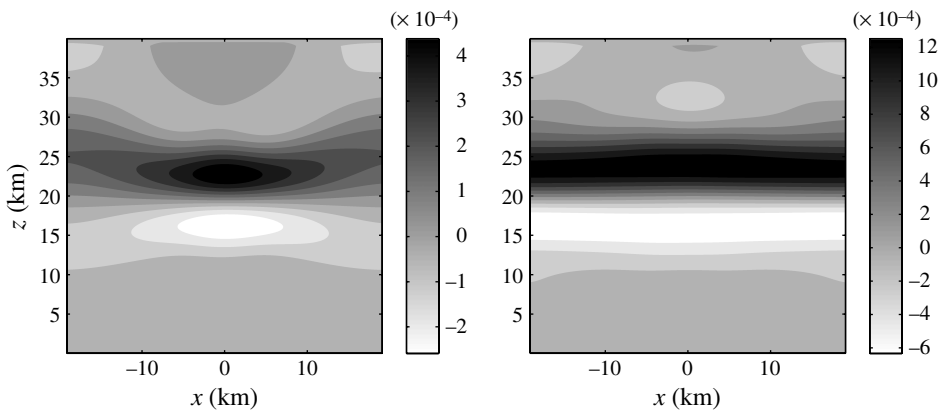
FIGURE 14. For the two-dimensional case in the standard setting (see the main text): amplitude maxima along z of buoyancy plotted against time for two waves: —, wave 2 with WKB; ––, wave 2 with the full model; –·–, wave 3 with the full model. Units are m s^{-2}. The various small parameters are $(\varepsilon, \varepsilon_1, \varepsilon_2) = (5.2 \times 10^{-3}, 5.2 \times 10^{-4}, 3.2 \times 10^{-2})$.

FIGURE 15. For the two-dimensional case in the standard setting (see the main text): spatial dependence of the mean horizontal velocity in the full model at $t = 5$ min and $t = 20$ min. Units are m s^{-1}. The various small parameters are $(\varepsilon, \varepsilon_1, \varepsilon_2) = (5.2 \times 10^{-3}, 5.2 \times 10^{-4}, 3.2 \times 10^{-2})$.

The mean horizontal velocity $U_0^{(0)}$ is shown in a Hovmöller diagram (figure 16a,b) and is in very good agreement. For the mean buoyancy derivative $\partial B_0^{(2)}/\partial x$ the contour plot at $t = 5$ min is shown (figure 16c,d). The shape of the signal slightly differs but magnitude and overall structure of the solution are also in good agreement. The same holds for the mean Exner pressure derivative $\partial \Pi_0^{(2)}/\partial x$ shown in figure 16(e,f).
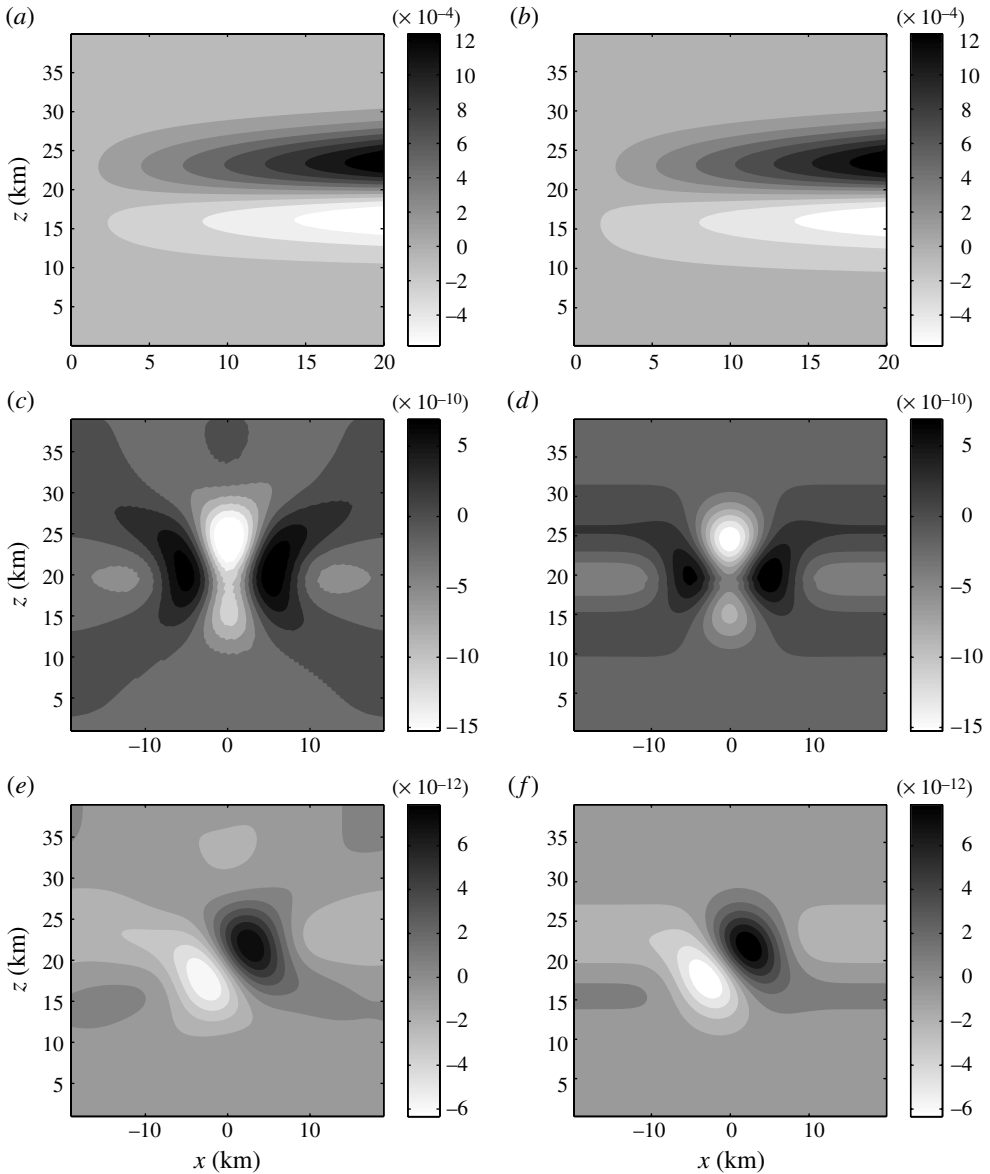
FIGURE 16. For the two-dimensional case in the standard setting (see the main text): comparison of the mean flow calculated with the full model (*a,c,e*) and the ray tracer (*b,d,f*). Hovmöller diagram of the mean horizontal velocity $U_0^{(0)}$ (*a,b*, in m s^{-1}); contour plot of the mean-flow buoyancy derivative $\partial B_0^{(2)}/\partial x$ (*c,d*, in s^{-2}) and contour plot of the mean Exner pressure derivative $\partial \Pi_0^{(2)}/\partial x$ (*e,f*, in m^{-1}) at $t = 5$ min. The various small parameters are $(\varepsilon, \varepsilon_1, \varepsilon_2) = (5.2 \times 10^{-3}, 5.2 \times 10^{-4}, 3.2 \times 10^{-2})$.

5.4. *Pseudo-incompressible versus anelastic model*

It is of interest to see the range of validity of sound-proof models, e.g. for the pseudo-incompressible system introduced by Durran (1999) and the most popular
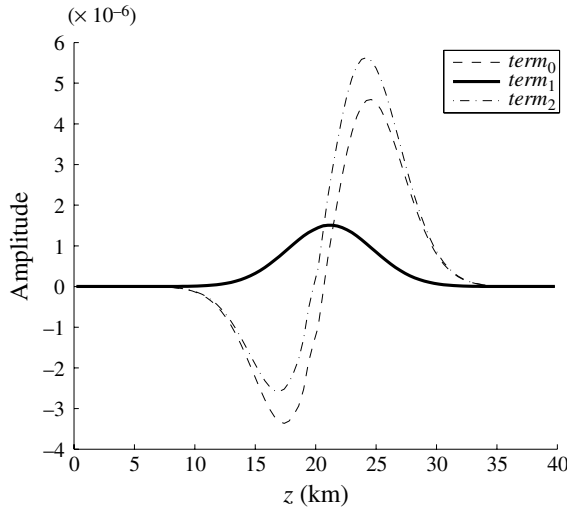
FIGURE 17. For the two-dimensional case in the standard setting (see the main text): line plot of various terms of the mean flow vertical momentum equation (5.4) at the horizontal domain centre $x = 0$ after $t = 20$ min. The thick solid line represents a buoyancy term present in the Euler and pseudo-incompressible equations, but which is absent in the anelastic theory. Units are m s^{-2}. The various small parameters are $(\varepsilon, \varepsilon_1, \varepsilon_2) = (5.2 \times 10^{-3}, 5.2 \times 10^{-4}, 3.2 \times 10^{-2})$.

anelastic model by Lipps & Hemler (1982). In the derivation of the extended WKB theory (Achatz *et al.* 2010) one difference became apparent in the mean vertical momentum equation

$$\underbrace{\theta^{(0)} c_p \frac{\partial \Pi_0^{(2)}}{\partial z} - B_0^{(2)}}_{term_0} + \underbrace{\frac{\left|B_1^{(1)}\right|^2}{2g}}_{term_1} = \underbrace{-\frac{1}{2\rho_0} \left\{ \frac{\partial \left[\rho_0 \mathscr{R}(u_1^{(0)} w_1^{(0)*})\right]}{\partial x} + \frac{\partial \left[\rho_0 |w_1^{(0)}|^2\right]}{\partial z} \right\}}_{term_2}. \quad (5.4)$$

The buoyancy $term_1$ appears in the full Euler equations as well as in the pseudo-incompressible equations but not in the anelastic model. We have investigated the actual relative magnitude of this term in the context of our test cases. For the present two-dimensional GWP test case after $t = 20$ min the answer can be found in figure 17 where $term_0$, $term_1$ and $term_2$ are plotted with different line styles. Note that we calculated $term_0$ as residue between $term_1$ and $term_2$ since the two components of $term_0$ cannot be determined individually as discussed in the previous section on mean flow. The buoyancy $term_1$ makes up $\sim 30\%$ of the left-hand side of the momentum balance (5.4). Note that this result was obtained in similar quality both with the full pseudo-incompressible model (not shown here) and with the WKB model.

6. Summary and conclusions

The range of validity of XWKB proposed by Achatz *et al.* (2010) has been examined. Central predictions of this large-amplitude theory are classic wave-action conservation and variation of local frequency and wave number by the eikonal

equations, but also the non-resonant forcing of higher harmonics of the basic gravity-wave field, mostly by large-scale gradients of the gravity-wave fluxes. For the time being, nonlinear wave–wave interactions (e.g. McComas & Bretherton 1977; Caillol & Zeitlin 2000; Lvov *et al.* 2012) are neglected. Eventually this will have to be amended, as Dunkerton (1987) has shown that such interactions can be important once a gravity wave propagates into a non-quiescent region. The theory so far has been obtained as a distinguished limit within multiple-scale asymptotics. The governing small parameter is the scale-separation ratio between the inverse wave number of the gravity wave and potential-temperature scale height. Based on linear theory it is assumed to be of the same order as the ratio between the leading-order amplitude of the gravity-wave potential-temperature fluctuations and the reference-state potential temperature. The validity of using linear theory in this estimate is corroborated by the fact that the leading-order equations in the present asymptotic regime are those also obtained in a linearized Boussinesq model. The assumptions of the distinguished limit are met as long as the non-dimensional wave amplitude a is close to the threshold for static instability, $a = O(1)$. The limit case $a = 1$, however, immediately leads to a turbulent wave breakdown so that we can only assume that a is somewhat less than 1. Finally, it was also assumed that gravity-wave amplitudes have the same spatial scale as the reference-atmosphere potential temperature. In reality this equality of scale- and amplitude-separation ratios is never met in purity so that a testing of the theory against typical cases seemed necessary. For this purpose the evolution of a GWP in a pseudo-incompressible model is compared with the predictions by XWKB.

To implement the reduced model a mixed Euler–Lagrangian approach is chosen. The wave action is treated as a conservative quantity on a finite-volume mesh using numerical flux functions for its transport. The rays carrying the wave properties frequency and wave number are dispersed over the finite-volume mesh and can move freely according to the ray equations. Cell-to-ray interpolation and ray-to-cell interpolation routines are applied to supply the Lagrangian and Euler method with the needed information.

The first part of the validation considers a simple one-dimensional GWP, i.e. with a Gaussian profile only in the vertical. This allows the straightforward application of the discrete fast Fourier transform (FFT) for horizontal slices. We first investigated the influence of the wavelength. Keeping the various ratios in constant relation, this allows for an investigation of how small the asymptotic control parameter actually needs to be in order to obtain useful results. For small wavelength $\lambda \leqslant 2$ km, with potential-temperature scale height ~ 30 km, and the gravity-wave envelope scale at 5 km, all predictions from asymptotic XWKB theory could be validated. The predictions for the basic wave 1 match nearly perfectly, while wave 2 shows a strong amplitude oscillation about the predicted behaviour. Finally, even when we increase the wavelength to values as high as the half-width of the wave packet, at least the wave 1 results were still very good. The qualitative behaviour predicted by XWKB can still be observed with the full-model calculations, i.e. the propagation speed of the wave packet, the mean amplitude of wave 2 and the absence of wave numbers greater than 2. Quantitatively, the results deviate as the wave packet evolves in time: for larger wavelengths the wave 1 energy is transferred to the kinetic energy of the mean flow much stronger than predicted by XWKB. Furthermore, wave 2 oscillates in the full model while XWKB predicts a smoothly developing value. Harmonics higher than 2 are present in the full model, albeit with a very small amplitude indicating a lower asymptotic order. Taking higher-order terms into account in the XWKB ansatz,

this behaviour might also be predicted by the XWKB theory. Further modifications might become necessary in the hydrostatic case $\lambda_x \gg \lambda_x$ or in the modulationally unstable case $\lambda_x \leqslant 0.7\lambda_z$ (Sutherland 2006). The results also depend on the amplitude a normalized with regard to the static stability threshold. The regime considered by Achatz *et al.* (2010) assumes $a = O(1)$, so that the typical parameter setting implies a disparity between the respective small parameters which the distinguished limit assumes to be of equal order. We varied a from 0.1 up to 1.0. The amplitude of wave 2 increases in proportion to the initial wave 1 amplitude and, in the same way, so do the oscillations. The larger the wave amplitude, the more the full-model mean falls behind the WKB amplitude prediction for increasing a. This, however, is a numerical effect: increasing amplitudes lead to stronger pronounced peaks which are damped by the upwind scheme. Finally the theory was also tested in longer integrations allowing significant wave–mean-flow interactions to develop. Up to the point of nonlinear wave dissipation XWKB was able to give at least qualitatively useful results. Beyond this point the XWKB code turned out to develop numerical instabilities. We suspect that at least one reason for this is the crossing of ray paths so that there is no unique phase more at a given location.

In the two-dimensional case we verified the results obtained in the one-dimensional test case for a reference test case setting. For this purpose we preprocessed the data in several steps which, in the end, stripped the data from the Gaussian profile and made it accessible to FFT. In addition we analysed the XWKB predictions for the mean-flow buoyancy and Exner pressure and could find good agreement between full and reduced model. Finally, we analysed the buoyancy term of the leading-order vertical momentum equation which is only predicted for Euler and pseudo-incompressible WKB and is absent in the WKB originating from the anelastic equations. It turned out that for the reference test case this term made up some 30 % of the balance. One should realize, however, that presently the importance of this deviation is not yet clear. This will have to be pursued further once the more interesting case of a rotating atmosphere is considered with mean-flow balance interacting with the gravity-wave field (Grimshaw 1975*a*)

In conclusion, this work gives us confidence that XWKB theory can be used, including its nonlinear extension, even if the assumptions of the distinguished limit are not met in purity. Important limitations of the theory, however, leave considerable work for the future. One of these is the neglect of resonant wave–wave interactions, another the assumed spatial scale separation between gravity wave and mean flow. This can become violated by the strong shears directly induced by the gravity wave (Dunkerton 1981, 1982). Yet another limitation, as noted above, is the assumption that at each location only one local wave number and frequency is to be found. Wave refraction, for example, leads to an immediate violation of this situation (Dunkerton 1984), and it cannot be excluded that such an effect can be caused by the nonlinear wave–mean-flow interaction itself which can be crucial for the stability of the GWP (Sutherland 2006; Dosser & Sutherland 2011). Work on corresponding extensions is underway and will be presented elsewhere. Moreover, we have highlighted the differences between Euler and pseudo-incompressible WKB on the one hand and anelastic WKB on the other. Again the pseudo-incompressible equations appear as the most trustworthy alternative, as compared with anelastic theory. How far this is of practical consequence, as recently questioned by (Smolarkiewicz & Szmelter 2011), remains to be seen. Even these authors, however, conclude that the pseudo-incompressible equations are highly reliable, and as a minimum they remain a

sound-proof cornerstone against which more simplified approaches can be safely tested.

Acknowledgements

Appendix

A.1. *Preprocessing of the data*

The preprocessing is depicted in figure 18(*a–g*). In the first step we pick for any z a horizontal cut through the computational domain. The aim is to get rid of the Gaussian amplitude so that a standard FFT routine can be applied to calculate the spectral components of the GWP.

To this end we need the envelope of the wave packet. It can be found by identifying the local maxima of the wave packet and their interpolation. It turns out that the given maxima are not very precise since the data points are not dense enough, see figure 18(*b*). To improve the position of the maxima and their amplitude we spline-interpolate the original data. A close up of a local maximum can be seen for the original data in figure 18(*b*) and for the interpolated data in figure 18(*c*).

The number of available maxima is doubled by taking the absolute value of the signal as depicted in figure 18(*d*). The local maxima are computed in figure 18(*e*) giving us a discrete set of points of the envelope. In figure 18(*f*) we interpolate the local maxima over the spatial coordinates of the original data set and obtain the envelope. In figure 18(*g*) the wave packet signal is divided by the envelope amplitude giving a constant-amplitude sinusoidal signal. A FFT window of size 2^n is chosen in figure 18(*h*), which finishes the preprocessing and the FFT routines can be applied. The spectral amplitude obtained thus for the chosen z is finally multiplied again with the envelope determined before so as to obtain an x-dependent amplitude. Redoing the analysis for all z yields the desired spatially dependent amplitudes.

A.1.1. *Test of preprocessing*

The quality of the preprocessing and spectral analysis can be seen in figure 19. The original two-dimensional GWP is initialized with a wave 1 of (normalized) amplitude 1.0, a wave 2 amplitude of 10^{-3} and a wave 3 amplitude of 10^{-4}. The analysis of the prepared GWP data with the preprocessing described above and the application of FFT shows that the wave 1 amplitude is overestimated by 1–2 %. Note that wave 1 amplitude was set to zero in the figure to better see the amplitude of the other wave numbers. Clearly the signal around wave number 1, k_1, is smeared out and some other spurious amplitudes at $k_1 \pm k_1/3$ and $k_1 \pm 2k_1/3$ appear. The capturing of wave 2 depends on the phase shift $\Delta\phi_{1\rightarrow 2}$ between waves 1 and 2. For a phase shift of $\Delta\phi_{1\rightarrow 2} = 0$ or π the analysis captures only 45 % of the input signal, see figure 19(*a*). For a phase shift of $\Delta\phi_{1\rightarrow 2} = \pm\pi/2$ (see figure 19*b*) the captured signal amplitude
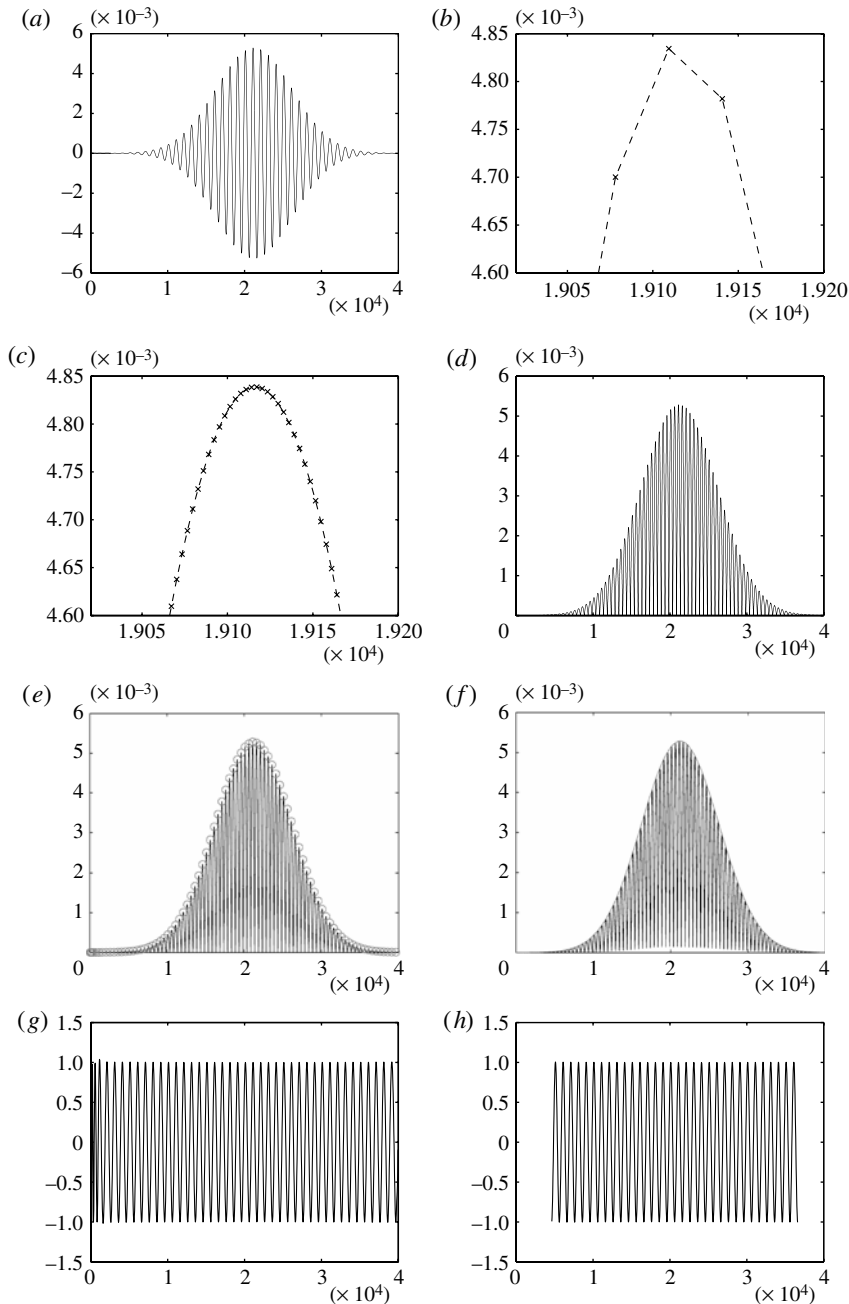
FIGURE 18. Preprocessing steps for analysing the Fourier modes in the two-dimensional GWP: (*a*) extract slice; (*b*), (*c*) spline-interpolate data set; (*d*) absolute value of GWP; (*e*) find local maxima; (*f*) interpolate maxima on the original data set to obtain envelope; (*g*) scale GWP with envelope; (*h*) choose FFT window.

is practically 100 % of the input data. The quality of the capturing of the wave 3 amplitude is practically not phase dependent and only varies 95 % and 100 %.
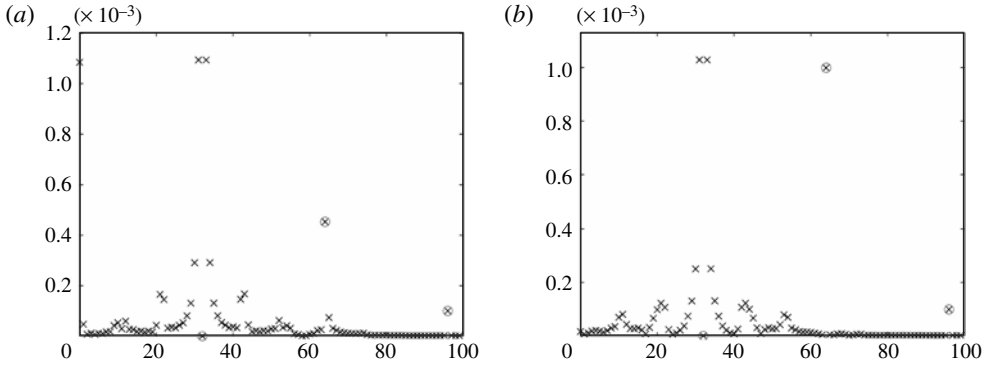
FIGURE 19. Spectrum of the GWP test data with preset amplitudes of waves 1, 2 and 3 calculated with preprocessing and FFT. The quality of the computed wave 2 amplitude depends on the phase shift between waves 1 and 2, $\Delta\phi_{1\to2}$. Shown are the computed spectra for $\Delta\phi_{1\to2} = 0$ (*a*) and $\Delta\phi_{1\to2} = \pm\pi/2$ (*b*). Note: that the amplitude of wave 1 was set to zero to better see the amplitudes of waves 2 and 3.

REFERENCES

ACHATZ, U. 2005 On the role of optimal perturbations in the instability of monochromatic gravity waves. *Phys. Fluids* **17**, 094107.

ACHATZ, U. 2007 Modal and nonmodal perturbations of monochromatic high-frequency gravity waves: primary nonlinear dynamics. *J. Atmos. Sci.* **64**, 1977–1994.

ACHATZ, U., KLEIN, R. & SENF, F. 2010 Gravity waves, scale asymptotics, and the pseudo-incompressible equations. *J. Fluid Mech.* **663**, 120–147.

ALEXANDER, M. J. & DUNKERTON, T. J. 1999 A spectral parameterization of mean-flow forcing due to breaking gravity waves. *J. Atmos. Sci.* **56**, 4167–4182.

ALEXANDER, M. J., GELLER, M., MCLANDRESS, C., POLAVARAPU, S., PREUSSE, P., SASSI, F., SATO, K., ECKERMANN, S., ERN, M., HERTZOG, A., KAWATANI, Y., PULIDO, M., SHAW, T. A., SIGMOND, M., VINCENT, R. & WATANABE, S. 2010 Recent developments in gravity-wave effects in climate models and the global distribution of gravity-wave momentum flux from observations and models. *Q. J. R. Meteorol. Soc.* **136**, 1103–1124.

BRETHERTON, F. P. 1966 The propagation of groups of internal gravity waves in a shear flow. *Q. J. R. Meteorol. Soc.* **92**, 466–480.

CAILLOL, P. & ZEITLIN, V. 2000 Kinetic equations and stationary energy spectra of weakly nonlinear internal gravity waves. *Dyn. Atmos. Oceans* **32** (2), 81–112.

DOSSER, H. V. & SUTHERLAND, B. R. 2011 Anelastic internal wave packet evolution and stability. *J. Atmos. Sci.* **68** (12), 2844–2859.

DUNKERTON, T. J. 1981 Wave transience in a compressible atmosphere. Part I: transient internal wave, mean-flow interaction. *J. Atmos. Sci.* **38** (2), 281–297.

DUNKERTON, T. J. 1982 Wave transience in a compressible atmosphere. Part III: the saturation of internal gravity waves in the mesophere. *J. Atmos. Sci.* **39** (5), 1042–1051.

DUNKERTON, T. J. 1984 Inertia–gravity waves in the stratosphere. *J. Atmos. Sci.* **41** (23), 3396–3404.

DUNKERTON, T. J. 1987 Effect of nonlinear instability on gravity-wave momentum transport. *J. Atmos. Sci.* **44** (21), 3188–3209.

DURRAN, D. R. 1989 Improving the anelastic approximation. *J. Atmos. Sci.* **46**, 1453–1461.

DURRAN, D. R. 1999 *Numerical Methods for Wave Equations in Geophysical Fluid Dynamics*. Springer.

FRITTS, D. C. & ALEXANDER, M. J. 2003 Gravity wave dynamics and effects in the middle atmosphere. *Rev. Geophys.* **41** (1), 1003.

FRITTS, D. C., VADAS, S. L., WAN, K. & WERNE, J. A. 2006 Mean and variable forcing of the middle atmosphere by gravity waves. *J. Atmos. Sol.-Terr. Phys.* **68**, 247–265.

GRIMSHAW, R. 1975*a* Internal gravity waves: critical layer absorption in a rotating fluid. *J. Fluid Mech.* **70**, 287–304.

GRIMSHAW, R. 1975*b* Nonlinear internal gravity waves in a rotating fluid. *J. Fluid Mech.* **71**, 497–512.

HINES, C. O. 1997 Doppler spread parameterization of gravity-wave momentum deposition in the middle atmosphere. Part 1. Basic formulation. *J. Atmos. Sol.-Terr. Phys.* **59**, 371–386.

HOLTON, J. R. 1982 The role of gravity wave induced drag and diffusion in the momentum budget of the mesosphere. *J. Atmos. Sci.* **39**, 791–799.

KEMM, F. 2010 A comparative study of TVD-limiters—well-known limiters and an introduction of new ones. *Intl J. Numer. Meth. Fluids* **67** (4), 404–440.

KIM, Y.-J., ECKERMANN, S. D. & CHUN, H.-Y. 2003 An overview of the past, present and future of gravity-wave drag parametrization for numerical climate and weather prediction models. *Atmos.-Ocean* **41**, 65–98.

KLEIN, R. 2009 Asymptotics, structure, and integration of sound-proof atmospheric flow equations. *Theor. Comput. Fluid Dyn.* **23**, 161–195.

KLEIN, R. 2010 Scale-dependent models for atmospheric flows. *Annu. Rev. Fluid Mech.* **42**, 249–274.

KLEIN, R. 2011 On the regime of validity of sound-proof model equations for atmospheric flows. *ESMWF Workshop on Non-hydrostatic Modelling,* 8–10 November 2010.

LINDZEN, R. S. 1981 Turbulence and stress owing to gravity wave and tidal breakdown. *J. Geophys. Res.* **86**, 9707–9714.

LIPPS, F. & HEMLER, R. 1982 A scale analysis of deep moist convection and some related numerical calculations. *J. Atmos. Sci.* **29**, 2192–2210.

LOMBARD, P. N. & RILEY, J. R. 1996 Instability and breakdown of internal gravity waves. I. Linear stability analysis. *Phys. Fluids* **8**, 3271–3287.

LVOV, Y. V., POLZIN, K. L. & YOKOYAMA, N. 2012 Resonant and near-resonant internal wave interactions. *J. Phys. Oceanogr.* **42** (5), 669–691.

MCCOMAS, C. H. & BRETHERTON, F. P. 1977 Resonant interaction of oceanic internal waves. *J. Geophys. Res.* **82**, 1397–1412.

MEDVEDEV, A. S. & KLAASSEN, G. P. 1995 Vertical evolution of gravity wave spectra and the parameterization of associated gravity wave drag. *J. Geophys. Res.* **100**, 25841–25853.

MÜLLER, P. 1976 On the diffusion of momentum and mass by internal gravity waves. *J. Fluid Mech.* **77**, 789–823.

RIEPER, F., HICKEL, S. & ACHATZ, U. 2013 A conservative integration of the pseudo-incompressible equations with implicit turbulence parameterization. *Mon. Weath. Rev.* **141**, 861–886.

SMOLARKIEWICZ, P. K. & SZMELTER, J. 2011 A nonhydrostatic unstructured-mesh soundproof model for simulation of internal gravity waves. *Acta Geophys.* **59** (6), 1109–1134.

SUTHERLAND, B. R. 2006 Weakly nonlinear internal gravity wavepackets. *J. Fluid Mech.* **569**, 249–258.

SUTHERLAND, B. R. 2010 *Internal Gravity Waves*. Cambridge University Press.

TORO, E. F. 1999 *Riemann Solvers and Numerical Methods for Fluid Dynamics, A Practical Introduction*, 2nd edn. Springer.